

DAQE: Enhancing the Quality of Compressed Images by Exploiting the Inherent Characteristic of Defocus

Qunliang Xing, *Graduate Student Member, IEEE*, Mai Xu, *Senior Member, IEEE*,
Xin Deng, *Member, IEEE*, and Yichen Guo

Abstract—Image defocus is inherent in the physics of image formation caused by the optical aberration of lenses, providing plentiful information on image quality. Unfortunately, existing quality enhancement approaches for compressed images neglect the inherent characteristic of defocus, resulting in inferior performance. This paper finds that in compressed images, significantly defocused regions have better compression quality, and two regions with different defocus values possess diverse texture patterns. These observations motivate our defocus-aware quality enhancement (DAQE) approach. Specifically, we propose a novel dynamic region-based deep learning architecture of the DAQE approach, which considers the regionwise defocus difference of compressed images in two aspects. (1) The DAQE approach employs fewer computational resources to enhance the quality of significantly defocused regions and more resources to enhance the quality of other regions; (2) The DAQE approach learns to separately enhance diverse texture patterns for regions with different defocus values, such that texture-specific enhancement can be achieved. Extensive experiments validate the superiority of our DAQE approach over state-of-the-art approaches in terms of quality enhancement and resource savings.

Index Terms—Image defocus, quality enhancement, compressed image, deep learning.

1 INTRODUCTION

NOWADAYS, we are embracing an era of the explosive growth of images. According to Domo statistics [1], Facebook stored and transmitted approximately 147,000 images per minute in 2020; similar situations were observed in other internet servers, such as WeChat and Twitter. To store and transmit such a large number of images, several lossy image compression standards, *e.g.*, joint photographic experts group (JPEG) [2], JPEG 2000 [3], and high-efficiency video coding with main still image profile (HEVC-MSP)/better portable graphics (BPG) [4], [5], have been successfully developed to reduce transmission bandwidths and storage costs. However, the compressed images suffer from compression artifacts, *e.g.*, ringing, blocking, and blurring effects [6], thus degrading the quality of user experience (QoE) [7], [8].

This paper proposes enhancing the quality of compressed images by taking into account the characteristic of image defocus, which is a blurring effect caused by the optical aberrations of lenses. Specifically, only regions close to the focal plane, *i.e.*, within the depth of field (DoF) [9], appear to be focused, while regions far from the focal plane are blurred [10]. Given the characteristic of image defocus, there are two main drawbacks of state-of-the-art approaches [11], [12], [13], [14], [15], [16], [17], [18], [19],

[20], [21], [22], [23], [24] regarding the quality enhancement of compressed images. **(1) Regionwise quality agnostic.** Existing approaches neglect the difference in the quality of different regions of an input image; thus, they process the whole image in the same manner. However, there exists a significant regionwise quality difference in a single compressed image, particularly referring to regions with different defocus values. **(2) Regionwise texture agnostic.** Existing approaches do not consider the texture difference in a compressed image. Consequently, they are not effective in enhancing diverse texture patterns, of which the diversity can also be reflected in their defocus values. Ideally, texture-specific quality enhancement should be conducted for diverse texture patterns, especially those of regions with different defocus values.

We address the above two drawbacks of existing approaches by utilizing inherent and off-the-shelf image defocus. We obtain two observations by analyzing the defocus and quality of compressed images from the diverse 2K resolution image (DIV2K) dataset [26], as shown in Figure 1. (1) The compression quality of compressed images is highly correlated with image defocus. Specifically, in a compressed image, significantly defocused regions have better compression quality than slightly defocused regions. Thus, regions with different defocus values in a compressed image should be separately enhanced. (2) Regions with different defocus values tend to have diverse texture patterns. Therefore, texture-specific enhancement can be achieved by separately enhancing regions with different defocus values.

Based on our observations, we propose a defocus-aware quality enhancement approach, named DAQE, for enhancing the quality of compressed images. The DAQE approach is equipped with a novel dynamic deep learning-based

- Q. Xing is affiliated with the School of Electronic Information Engineering and the Shen Yuan Honors College, Beihang University, Beijing, China. E-mail: xingql@buaa.edu.cn.
- M. Xu and Y. Guo are affiliated with the School of Electronic Information Engineering, Beihang University, Beijing, China. E-mail: {maixu, gyc970930}@buaa.edu.cn.
- X. Deng is affiliated with the School of Cyber Science and Technology, Beihang University, Beijing, China. E-mail: cindyding@buaa.edu.cn.
- Corresponding author: Mai Xu.

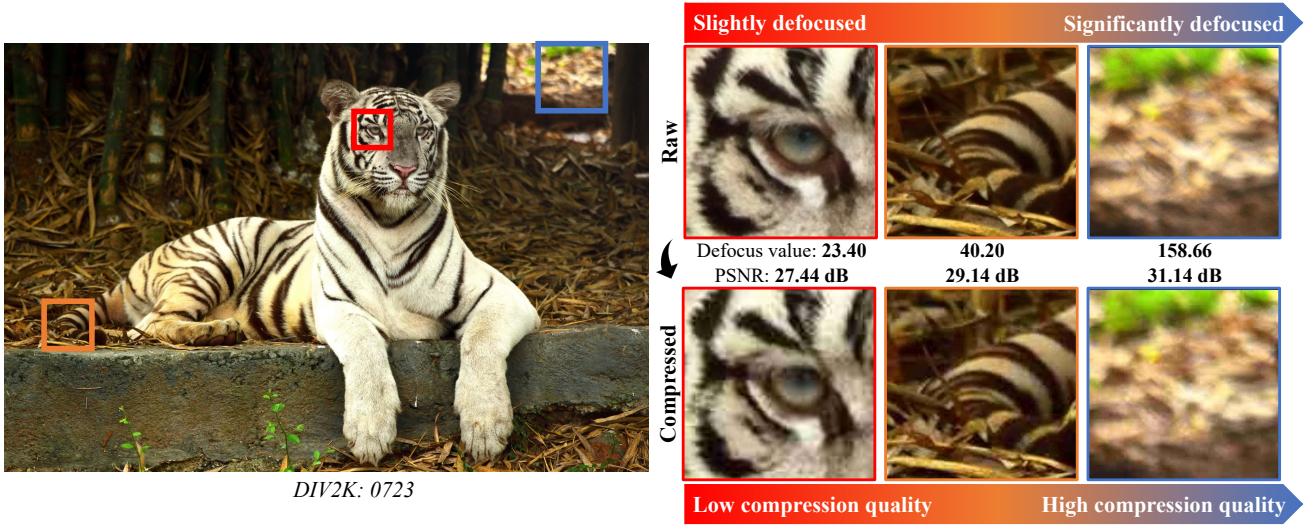


Fig. 1. Motivation of our DAQE approach. There exist regions with different defocus values within an image. The defocus values are estimated by the defocus map estimation network (DMENet) [25]. The image is compressed by JPEG [2] with the quality factor (QF) as 20.

architecture. First, the DAQE approach estimates the defocus map for the input image. Then, the DAQE approach conducts patchwise dynamic enhancement for patches with different defocus values separately. Considering that significantly defocused patches have superior compression quality compared with slightly defocused patches, the DAQE approach employs fewer computational resources to enhance the quality of significantly defocused patches and more resources on other patches to improve efficiency. Note that all patches are enhanced with a single dynamic architecture in an “easy-to-hard” manner. Additionally, the DAQE approach extracts diverse texture patterns for patches with different defocus values by embedding a unique attention-based texture learner in each enhancement path. The texture learner is designed to extract texture patterns diverse in shape and intensity. In this way, we can achieve texture-specific quality enhancement with improved efficacy.

Finally, we conduct extensive experiments to validate the effectiveness of our DAQE approach in terms of quality enhancement and resource savings, which is significantly better than state-of-the-art approaches. Furthermore, we demonstrate the effectiveness of utilizing defocus for quality enhancement in two aspects: (1) Explicitly clustering patches with different quality is effective for enhancing the quality of compressed images, which can be approached efficiently by using image defocus; (2) Explicitly reasoning about defocus reduces the difficulty of finding relevance among global patches. Our demonstrations explain the success of DAQE for quality enhancement of compressed images, and also have the potential to inspire other regionwise image enhancement works.

2 RELATED WORKS

2.1 Quality Enhancement of Compressed Images

During the past decade, many deep learning-based approaches [11], [12], [13], [15], [16], [20] have been proposed for enhancing the quality of compressed images, owing to

the successful development of convolutional neural networks (CNNs) [27]. Specifically, Dong *et al.* [11] proposed a shallow four-layer artifact reduction CNN (AR-CNN), pioneering CNN-based quality enhancement approaches for JPEG-compressed images. Later, approaches with deeper CNN structures and the quantization prior of JPEG compression, *i.e.*, deep dual-domain (D3) [13] and deep dual-domain CNN (DDCN) [12], were proposed to remove JPEG compression artifacts. Wang *et al.* [16] proposed a 10-layer deep CNN-based auto decoder (DCAD), which is the first CNN-based quality enhancement approach for BPG-compressed images. DCAD does not utilize coding information from codecs but surpasses most previous approaches in terms of the quality of enhanced images thanks to the effective learning structure of a much deeper network. To take a step forward, the denoising convolutional neural network (DnCNN) [15] was proposed, which combines a 20-layer deep network with advanced techniques of the day including residual learning [28] and batch normalization [29]. In this way, DnCNN significantly outperforms most traditional model-based approaches such as block-matching and 3-D filtering (BM3D) [30], as well as the above learning-based approaches. Most recently, Xing *et al.* [20] proposed a resource-efficient blind quality enhancement (RBQE) approach for both JPEG-compressed and BPG-compressed images. The RBQE approach was designed with a dynamic inference structure, such that blind yet effective quality enhancement can be achieved for compressed images. In this paper, we propose utilizing image defocus for the quality enhancement of compressed images.

2.2 Defocus-Aware Vision Tasks

In this section, we review defocus-aware works of related vision tasks. The characteristic of image defocus provides plentiful information about image quality, depth, objectness, saliency, *etc.* Hence, image defocus has been widely used in many vision tasks, *e.g.*, image depth estimation [31], [32], [33], [34], image defocus deblurring [35], [36], [37], image

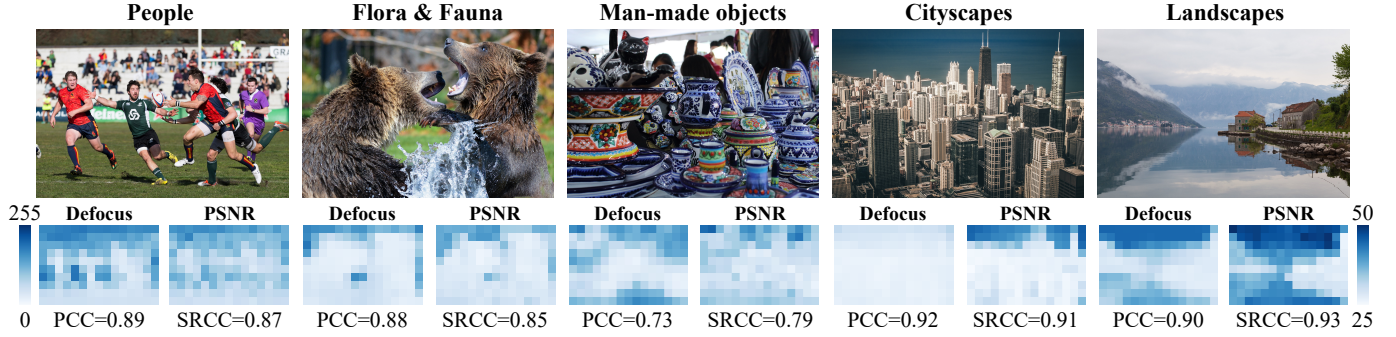


Fig. 2. Correlation between the patchwise defocus and PSNR (dB) values within a single image. Five example images from the DIV2K dataset with different contents are presented. The left color bar is for defocus maps, while the right one is for PSNR maps. Images are compressed by the BPG codec with the quantization parameter (QP) as 37.

saliency detection [38], [39], and image segmentation [40]. For image depth estimation, Pentland *et al.* [31] showed that two images formed with different apertures indicate depth information. Thus, the image depth can be generated from image defocus. For image defocus deblurring, the works of [35], [36], [37] are relevant, in which the defocus kernel is estimated and then used to deblur images. For image saliency prediction, Jiang *et al.* [39] found that salient image regions are often photographed in focus; therefore, the estimation of image defocus maps can boost the performance of higher-level saliency prediction.

To the best of our knowledge, no works consider defocus-aware quality enhancement for compressed images. In addition, the correlation between the region quality and region defocus of compressed images is unclear. In this paper, we thoroughly investigate this correlation and demonstrate that the characteristic of image defocus can significantly benefit quality enhancement by our proposed DAQE approach.

3 OBSERVATIONS

This section presents our observations on how the characteristic of defocus is related to the regionwise quality and texture patterns of the compressed images. Our observations are obtained by analyzing a widely used DIV2K dataset [26], which includes 900 images with 2K resolution. These images cover a large diversity of contents, including people (13.67%), flora and fauna (31.56%), man-made objects (19.11%), cityscapes (20.78%), and landscapes (14.89%), as shown in Figure 2. In addition, these images can also fall into the scenes of indoor (11.89%), outdoor (83.89%), and underwater (4.22%). First, to evaluate the defocus level for each image, we adopt state-of-the-art DMENet [25] to generate a defocus map for each image.¹ Then, to obtain compressed images, we compress all images with two compression codecs (*i.e.*, the BPG [5] and JPEG [2] codecs) and eight settings (*i.e.*, with a quantization parameter (QP) [4] of 27/32/37/42 or a quality factor (QF) of 20/30/40/50). Next, to evaluate the regionwise defocus, quality, and texture patterns, we crop all images and defocus maps into

1. A defocus map is an eight-bit grayscale image ranging from 0 to 255. Pixels with larger defocus values are estimated to be further away from the focal plane.

TABLE 1
Variation in the patchwise defocus values within a single image.

Content	People	Flora&Fauna	Man-made	Cityscapes
STD	34.26	39.13	26.06	37.79
Mean	64.64	69.99	50.00	55.17
CV (%)	50.16	54.74	46.67	61.10
Range	129.16	135.84	107.26	130.67

Content	Landscapes	Indoor	Outdoor	Underwater
STD	34.81	24.85	36.67	31.44
Mean	52.99	52.99	60.91	57.58
CV (%)	60.66	41.57	56.82	51.34
Range	127.07	103.36	130.69	122.24

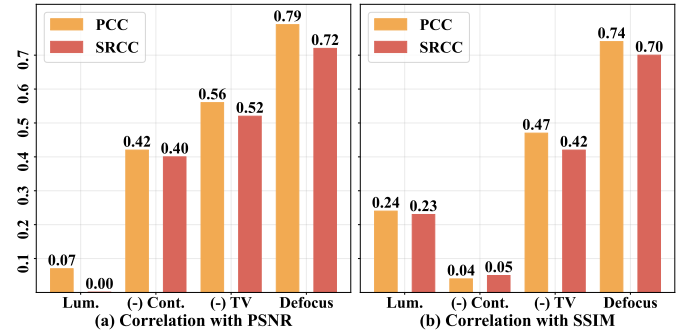


Fig. 3. Correlation between patch quality and features. The “lum” and “cont” are the abbreviations of “luminance” and “contrast”.

nonoverlapping patches with size 128×128 . Finally, we calculate the average defocus value for each patch as the patchwise defocus value.

Observation 1: There exists dramatic variation in the patchwise defocus values within a single image.

Analysis: We measure the variation in the patchwise defocus values in a single image in terms of the standard deviation (STD), coefficient of variation (CV) [41], and range. Specifically, the CV value is the ratio of the STD value to the mean value. The range value is obtained by subtracting the lowest patchwise defocus value from the highest value within an image. As shown in Table 1, the CV value is no less than 40% for all contents, indicating a strong variation in patchwise defocus values. In addition, the defocus range

is up to 135.84 (*i.e.*, for Flora & Fauna), which is nearly two times the corresponding mean value (*i.e.*, 69.99). Similar results can be found for other contents in Table 1, implying a large interval of the patchwise defocus values within each image. Thus, the variation in patchwise defocus values within a single image is dramatic. Intuitively, a shallow DoF is typically preferred by photographers to produce high-quality images, causing the difference in patchwise defocus values. Hence, the widely-used DIV2K benchmark for quality enhancement can exhibit such a large variation in the patchwise defocus values. Finally, the analysis of Observation 1 is accomplished.

Observation 2: For a compressed image, patches with higher defocus values tend to have better compression quality.

Analysis: We adopt two widely-used quality assessment metrics, *i.e.*, the peak signal-to-noise ratio (PSNR) and structural similarity index measure (SSIM) [42], for measuring the compression quality. Then, for each compression setting, the Pearson correlation coefficient (PCC) [43] and Spearman’s rank correlation coefficient (SRCC) [44] values are calculated between the defocus and quality values for all patches, to validate their correlation. The results are then averaged by eight compression settings. In addition to the defocus, we adopt the features of luminance, contrast, and total variation (TV) as the baseline. As shown in Figure 3, both the PSNR and SSIM values of patches are highly correlated with their corresponding defocus values. Specifically, both the PCC and SRCC values between quality and defocus are above 0.70, significantly higher than those between quality and baseline features. Some examples are shown in Figure 2. Consequently, defocus can serve as a good indicator for regionwise compression quality (measured by PSNR and SSIM). More importantly, the correlation between defocus and quality is positive, implying superior compression quality for patches with higher defocus values. In fact, for better rate-distortion performance, image compression is mainly performed on high-frequency components [2], [4]; as a result, patches with higher defocus values tend to have better compression quality due to the weakened high-frequency components caused by defocus. Finally, the analysis of Observation 2 is accomplished.

Observation 3: For a compressed image, the texture patterns of the patches with dissimilar defocus values are more diverse than those with similar defocus values.

Analysis: We cluster all patches into three clusters by the K-means clustering algorithm [45], [46] according to their defocus values. Figure 4 shows that the patches in different clusters can differ significantly in quality, which accords with Observation 2. Here, we further measure the average texture difference between patches in the same/different clusters. Specifically, the texture difference of two patches is measured by the Frobenius norm of the difference between their Gram matrices of Y components, named the texture difference index measure (TDIM), which has been widely used in many texture-related works [47], [48]. Note that larger TDIM values indicate more diversity in the texture patterns between two patches. As shown in Figure 5, the TDIM values between patches in two different clusters are much larger than those between patches in the same cluster. For example, for images compressed at QP = 37,

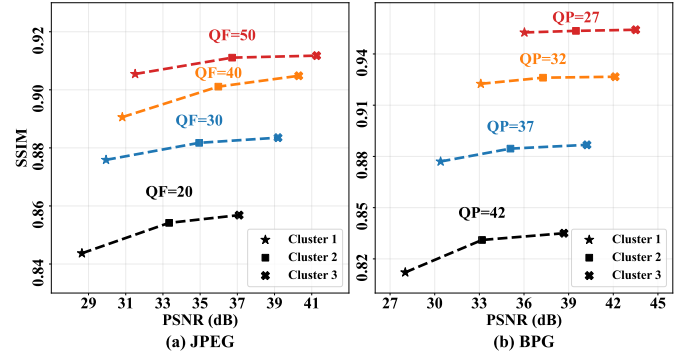


Fig. 4. Average patch quality of three clusters in terms of PSNR (dB) and SSIM.

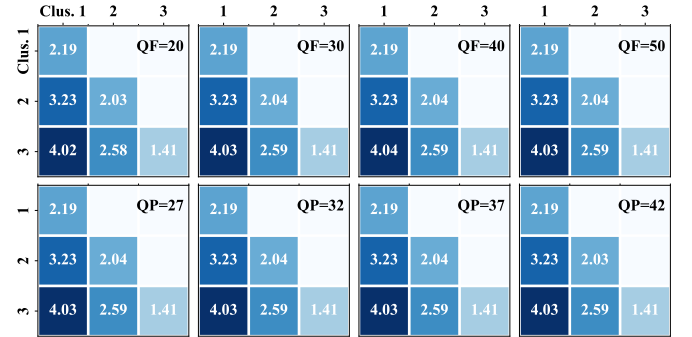


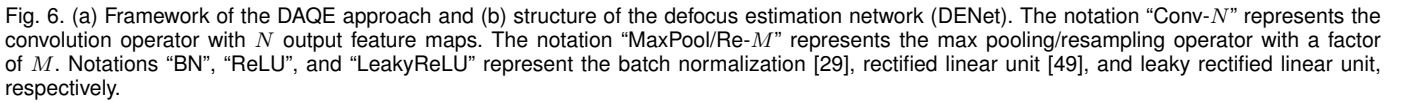
Fig. 5. Texture difference between three clusters. The “clus” is the abbreviation of “cluster”. The texture difference is measured by the TDIM value ($\times 10^3$).

the average TDIM value between two patches in the first cluster is 2.19×10^3 , significantly lower than that between two patches in clusters 1 and 3 (*i.e.*, 4.03×10^3). Therefore, for a compressed image, the texture patterns of patches with dissimilar defocus values are more diverse than those with similar defocus values. Intuitively, the patches with dissimilar defocus values are blurred more diversely; consequently, their texture patterns are also blurred more diversely than those with similar defocus values. Finally, the analysis of Observation 3 is accomplished.

4 PROPOSED APPROACH

In this section, we focus on our proposed DAQE approach for enhancing the quality of compressed images. The DAQE approach aims to enhance the quality of regions with different defocus values. Considering that these regions differ significantly in compression quality and texture patterns (as illustrated by Observations 2 and 3), we implement the DAQE approach by proposing an enhancement framework with three main steps as shown in Figure 6 (a), *i.e.*, defocus estimation, attention generation, and dynamic quality enhancement.

Specifically, (1) the DAQE approach first estimates the defocus value for each image patch with a proposed defocus estimation network (DENet). (2) Then, the DAQE approach divides patches into N clusters according to their defocus values, and conducts cluster-specific texture extraction and quality enhancement. To extract the texture pattern for each



4.1 Defocus Estimation

can facilitate the cross-domain learning of image defocus estimation (*i.e.*, from the image domain to the defocus feature domain), as inspired by DMENet [25]. Finally, a U-Net [52]-based decoder, denoted by $D_{\text{U-Net}}$, is adopted followed by a series of residual blocks R_{out} , for generating the defocus map \mathbf{M} from \mathbf{F}_{VG} . Mathematically, we can obtain the defocus map \mathbf{M} for the input compressed image \mathbf{I}_{in} as follows:

$$\mathbf{M} = R_{\text{out}}(D_{\text{U-Net}}(E_{\text{VGG}}(R_{\text{clean}}(\mathbf{I}_{\text{in}})))), \quad (1)$$

where \mathbf{M} and \mathbf{I}_{in} have the same resolution.

Recall that the patchwise defocus value is the average defocus value for each patch. Therefore, we can obtain the patchwise defocus value for each patch, by first dividing \mathbf{M} into nonoverlapping $S \times S$ patches together with \mathbf{I}_{in} and then calculating the average of the corresponding patch of \mathbf{M} .

4.2 Defocus-Aware Attention Generation

In our DAQE approach, we design AGNet to extract the texture pattern for an input patch. The attention mechanism [53] has been widely used to extract texture patterns for image quality enhancement and other restoration tasks [54], [55], [56], [57], [58]. However, the various implementations of the attention mechanism in these works are conducted over the whole image, neglecting the texture diversity of different regions. As shown in Figure 7 (a), AGNet mitigates this drawback by implementing the attention mechanism for regions with different defocus values separately, as those regions differ significantly in texture patterns, as discussed in Observation 3. Specifically, AGNet first divides all patches into N_{clu} clusters according to their defocus values. Then, for each input patch, AGNet captures (1) local attention to the input patch and (2) global attention

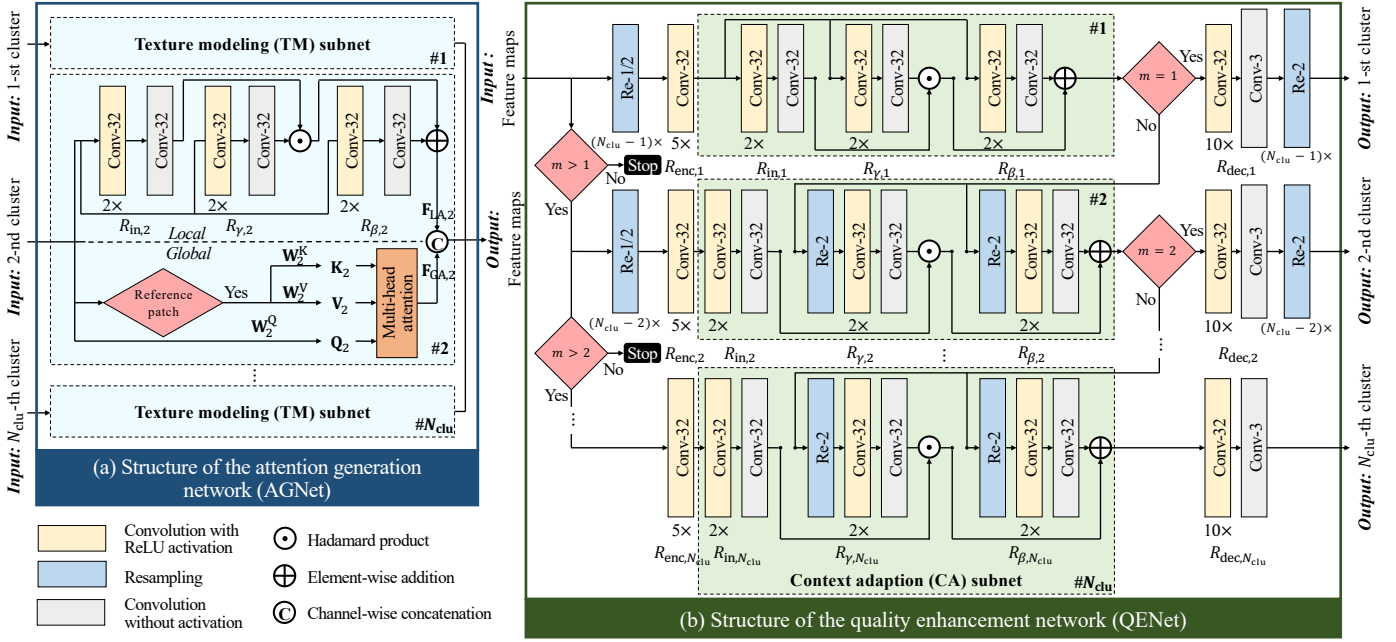


Fig. 7. Structures of the (a) attention generation network (AGNet) and (b) quality enhancement network (QENet). The notation “Conv- N ” represents the convolution operator with N output feature maps. The notation “Re- M ” represents the resampling operator with a factor of M . The notation “ReLU” represents the rectified linear unit [49].

to reference patches in the same cluster. Finally, AGNet encodes and normalizes the input patch with both the captured local and global attention, such that the texture pattern of the input patch can be obtained.

Patch clustering. AGNet first divides all patches of an input image into N_{clu} clusters according to their defocus values. First, the defocus value centers of clusters are determined by the K-means algorithm [45], [46] over a large-scale dataset. Then, every patch is assigned to its closest cluster, in terms of the sum-of-squares distances between its defocus value and the center defocus values. In this way, AGNet can cluster the patches of the input image into different clusters with different defocus centers. Notably, according to Observation 3, patches in different clusters possess diverse texture patterns. This observation is utilized in the following attention generation.

Local attention generation. As mentioned above, the attention mechanism has been widely used to extract texture patterns for image quality enhancement and other restoration tasks. Inspired by the spatial adaptive normalization layer [56], our AGNet includes a texture modeling subnet (TM subnet) for each cluster of patches, to extract the texture pattern for an input patch, as illustrated in Figure 7 (a). We take the m -th TM subnet as an example, which processes the input patches in the m -th cluster, denoted by \mathbf{P}_m . First, \mathbf{P}_m is convolved by residual blocks $R_{in,m}$ to obtain the encoded feature $R_{in,m}(\mathbf{P}_m)$. Then, \mathbf{P}_m is convolved by residual blocks $R_{\gamma,m}$ and $R_{\beta,m}$, such that the corresponding attention maps $R_{\gamma,m}(\mathbf{P}_m)$ and $R_{\beta,m}(\mathbf{P}_m)$ can be produced. Then, $R_{in,m}(\mathbf{P}_m)$ is elementwise multiplied by $R_{\gamma,m}(\mathbf{P}_m)$ and then added by $R_{\beta,m}(\mathbf{P}_m)$ to generate the final output $\mathbf{F}_{LA,m}$. Mathematically, the above processes can be written as follows:

$$\mathbf{F}_{LA,m} = R_{in,m}(\mathbf{P}_m) \odot R_{\gamma,m}(\mathbf{P}_m) + R_{\beta,m}(\mathbf{P}_m). \quad (2)$$

Note that patches in the same cluster share a TM subnet, *i.e.*, with shared parameters, while those in different clusters are fed into different TM subnets, *i.e.*, with different sets of parameters that are learned separately. The reason is that the texture patterns of the patches in different clusters are more diverse than those in the same cluster.

Global attention generation. Observation 3 reveals that the texture patterns of patches in the same cluster are more similar than those of patches in different clusters. In light of this observation, AGNet includes a global branch in addition to the local branch for each TM subnet to take advantage of patches in the same cluster. As depicted in Figure 7 (a), the global branch works through the following steps.

- 1) N_{ref} patches are proposed as the global reference patches [59], which generate the key/value pairs for the queries of all patches in their same cluster. AGNet first uniformly samples \mathbf{I}_{in} to generate the initial reference patches, with a spatial sampling interval of $4S$ in both directions. Assume the height and width of \mathbf{I}_{in} are H and W , respectively. Then, we have N_{ref} global reference patches, and N_{ref} is equivalent to $H_s \times W_s$, where $H_s = \lfloor H / (4S) \rfloor$ and $W_s = \lfloor W / (4S) \rfloor$.
- 2) AGNet adjusts the positions $\{(x_i, y_i)\}_{i=1}^{N_{ref}}$ of the initial reference patches by adding the position offsets $\{(\Delta x_i, \Delta y_i)\}_{i=1}^{N_{ref}}$. Here, $\{(\Delta x_i, \Delta y_i)\}_{i=1}^{N_{ref}}$ can be learned in the form of an offset map \mathbf{F}_{offset} through an offset learning subnet as follows:

$$\mathbf{F}_{offset} = C_{1 \times 1}(L_{GELU}(C_{DW}(\mathbf{I}_{in}))), \quad (3)$$

where $C_{1 \times 1}$, L_{GELU} , and C_{DW} denote a convolution layer with a kernel size of 1×1 , a GELU activation layer [60], and a depthwise convolution layer,

respectively. Note that $\mathbf{F}_{\text{offset}}$ is a map with size $H_s \times W_s$, in which each element denotes the offset pair $(\Delta x_i, \Delta y_i)$ for the i -th reference patch.

- 3) AGNet performs differentiable sampling to obtain reference patches based on the initial reference patches $\{\mathbf{P}_{\text{init}}^{(i)}\}_{i=1}^{N_{\text{ref}}}$ and the offset map $\mathbf{F}_{\text{offset}}$. Specifically, a reference patch $\mathbf{P}^{(i)}$ located at $(x_i + \Delta x_i, y_i + \Delta y_i)$ can be obtained by bilinearly sampling $\{\mathbf{P}_{\text{init}}^{(i)}\}_{i=1}^{N_{\text{ref}}}$ as follows:

$$\mathbf{P}^{(i)} = \sum_{j=1}^{N_{\text{ref}}} g(x_i + \Delta x_i, x_j, W_s) g(y_i + \Delta y_i, y_j, H_s) \mathbf{P}_{\text{init}}^{(j)}, \quad (4)$$

where $g(a, b, c) = 1 - |a - b|/c$. In this way, the acquisition of reference patches can be differentiable and trained in an end-to-end manner.

- 4) Given the reference patches, AGNet computes the query of every input patch and the key/value pairs of the reference patches for each cluster as follows:

$$\mathbf{Q}_m = \tilde{\mathbf{P}}_m \mathbf{W}_m^Q, \quad (5)$$

$$\mathbf{K}_m^{(i)} = \tilde{\mathbf{P}}_m^{(i)} \mathbf{W}_m^{K,(i)}, i = 1, 2, \dots, N_{\text{ref}}^m, \quad (6)$$

$$\mathbf{V}_m^{(i)} = \tilde{\mathbf{P}}_m^{(i)} \mathbf{W}_m^{V,(i)}, i = 1, 2, \dots, N_{\text{ref}}^m. \quad (7)$$

In the above equations, $\tilde{\mathbf{P}}_m$ and $\tilde{\mathbf{P}}_m^{(i)}$ are the flattened \mathbf{P}_m and the flattened i -th reference patch $\mathbf{P}_m^{(i)}$ in the m -th cluster, respectively; \mathbf{W}_m^Q , $\mathbf{W}_m^{K,(i)}$ and $\mathbf{W}_m^{V,(i)}$ are the projection matrices for the query, key, and value, respectively; N_{ref}^m is the number of reference patches in the m -th cluster; \mathbf{Q}_m , $\mathbf{K}_m^{(i)}$ and $\mathbf{V}_m^{(i)}$ are the query of \mathbf{P}_m , key of $\mathbf{P}_m^{(i)}$, and value of $\mathbf{P}_m^{(i)}$, respectively. If N_{ref}^m is equivalent to 0, we choose the reference patch in the neighboring cluster with the defocus value closest to the center of this cluster.

- 5) AGNet performs multihead attention between \mathbf{Q}_m and each $(\mathbf{K}_m^{(i)}, \mathbf{V}_m^{(i)})$ pair. The attention output \mathbf{Z}_m of each attention head can be formulated as,

$$\mathbf{Z}_m = \sum_{i=1}^{N_{\text{ref}}^m} \sigma \left(\mathbf{Q}_m \mathbf{K}_m^{(i)\top} / \sqrt{d} + B \right) \mathbf{V}_m^{(i)}. \quad (8)$$

In the above equation, σ denotes the softmax function; d is the dimension of each head; B denotes the deformable relative position bias [59].

Finally, $\mathbf{F}_{\text{GA},m}$ is generated by the multihead attention, which is then concatenated with $\mathbf{F}_{\text{LA},m}$, *i.e.*, the output of the local branch. This operation results in the output feature $\mathbf{F}_{\text{out},m}$, which encodes the texture pattern for the input patch \mathbf{P}_m via both local and global attention. $\mathbf{F}_{\text{out},m}$ is then sent to QENet as introduced in the next section.

4.3 Defocus-Aware Dynamic Quality Enhancement

Given the estimated defocus value (Section 4.1) and extracted texture pattern (Section 4.2) for the input patch, our DAQE approach can finally conduct patchwise dynamic quality enhancement via the proposed QENet, as presented in the following.

Dynamic structure with multilevel enhancement. The texture patterns in different clusters are more diverse than

those in the same cluster, as revealed in Observation 3. It is therefore effective to enhance different clusters of patches in a “divide-and-conquer” manner to finely restore the diverse texture patterns. To this end, we equip QENet with a multilevel enhancement structure, which has N_{clu} levels of enhancement paths as shown in Figure 7 (b). In this dynamic structure, the input feature can be enhanced through different levels of paths, which are determined dynamically according to their defocus values. These paths are not independent; instead, they are connected progressively through context adaptation (CA) subnets. Specifically, the feature of each path is adapted to the context information provided by the upper path to take advantage of the similarity in texture patterns between these two neighboring clusters. QENet is resource-efficient in the following two aspects. (1) Defocus-aware progressive enhancement. The input features of patches with lower defocus values are enhanced via more levels of paths since they have inferior compression quality, as observed in Observation 2. In the most sophisticated case, all levels of paths are traversed from top to bottom to achieve optimal enhancement performance. Conversely, those with higher defocus values are enhanced by traversing only upper-level paths, so computational resources can be saved while maintaining high quality. (2) Dynamic resolution of inference feature. The input feature is downsampled by different factors at different levels before enhancement. The enhanced image is finally upsampled to restore the resolution. In this way, the upper-level enhancement is conducted over smaller inference features, thus consuming fewer computational resources.

Quality enhancement at each level. Here, we take the enhancement of the input feature $\mathbf{F}_{\text{in},m}$ as an example, where m is the cluster index. Note that a cluster with a smaller m has a higher center defocus value. Let n denote the level of the enhancement path. Then, the paths of the top- m levels are progressively traversed by $\mathbf{F}_{\text{in},m}$, *i.e.*, level n ranges from 1 to m . Specifically, at the n -th level of enhancement, $\mathbf{F}_{\text{in},m}$ is first downsampled by a factor of 2 ($N_{\text{clu}} - n$) times. Then, the downsampled feature is encoded by residual blocks $R_{\text{enc},n}$ into $\mathbf{F}_{\text{enc},m}^n$ as follows:

$$\mathbf{F}_{\text{enc},m}^n = R_{\text{enc},n} \left(\underbrace{\text{Dw}(\dots \text{Dw}(\mathbf{F}_{\text{in},m})) \dots}_{(N_{\text{clu}} - n) \text{ times}} \right), \quad (9)$$

where Dw is a downsampling operator with a factor of 1/2. Subsequently, $\mathbf{F}_{\text{enc},m}^n$ is further processed by the CA subnet to adapt $\mathbf{F}_{\text{enc},m}^n$ to a context feature and generate an adapted feature $\mathbf{F}_{\text{ada},m}^n$. For the top-level path, $\mathbf{F}_{\text{enc},m}^1$ serves as the context feature; for other paths, the output of the CA subnet at the upper path $\mathbf{F}_{\text{ada},m}^{n-1}$ serves as the context feature. The CA subnet first convolves $\mathbf{F}_{\text{enc},m}^n$ by a few residual blocks $\tilde{R}_{\text{in},n}$. It then convolves the context feature by residual blocks $\tilde{R}_{\gamma,n}$ and $\tilde{R}_{\beta,n}$ to obtain the adaptation maps $\mathbf{F}_{\gamma,m}^n$ and $\mathbf{F}_{\beta,m}^n$, respectively. The adapted feature $\mathbf{F}_{\text{ada},m}^n$ is produced by multiplying $\mathbf{F}_{\gamma,m}^n$ and then adding $\mathbf{F}_{\beta,m}^n$ to the convolved $\mathbf{F}_{\text{enc},m}^n$. The above processes can be written as follows:

$$\mathbf{F}_{\text{ada},m}^n = \tilde{R}_{\text{in},n}(\mathbf{F}_{\text{enc},m}^n) \odot \tilde{R}_{\gamma,n}(\mathbf{F}_{\text{ada},m}^{n-1}) + \tilde{R}_{\beta,n}(\mathbf{F}_{\text{ada},m}^{n-1}), \quad (10)$$

where $\mathbf{F}_{\text{ada},m}^0$ refers to $\mathbf{F}_{\text{enc},m}^1$. If the level index n meets the cluster index m , $\mathbf{F}_{\text{ada},m}^n$ is further sent to the decoder,

i.e., a set of residual blocks $R_{\text{dec},n}$, and then upsampled to generate the enhanced patch $\mathbf{P}_{\text{out},m}$ as follows:

$$\mathbf{P}_{\text{out},m} = \underbrace{\text{Up}(\cdots (\text{Up}(R_{\text{dec},n}(\mathbf{F}_{\text{ada},m}^n))) \cdots)}_{(N_{\text{clu}}-n) \text{ times}}, \quad (11)$$

where Up is an upsampling operator with a factor of 2. Finally, we can obtain the output enhanced image \mathbf{I}_{out} for the input compressed image \mathbf{I}_{in} by spatially combining all enhanced patches of all clusters.

4.4 Loss Functions

We train our DAQE model in a supervised manner. Here, we discuss the loss functions for supervision, which are composed of a quality enhancement loss and a defocus estimation loss.

Quality enhancement loss. Let \mathcal{L}_{en} denote the quality enhancement loss. Here, \mathcal{L}_{en} is modeled by the Charbonnier loss function [61] between the enhanced patch \mathbf{P}_{out} and the corresponding raw patch $\hat{\mathbf{P}}$,

$$\mathcal{L}_{\text{en}} = \sqrt{\|\mathbf{P}_{\text{out}} - \hat{\mathbf{P}}\|_2^2 + \epsilon^2}, \quad (12)$$

where ϵ is a hyperparameter for numerical stability. Then, AGNet and QENet are trained in an end-to-end manner by minimizing \mathcal{L}_{en} .

Defocus estimation loss. We also take into account the defocus estimation loss \mathcal{L}_{de} for training DENet. Ideally, the ground truth defocus map for the compressed image is available for supervision. Unfortunately, it is impossible to obtain the ground-truth defocus map for an image. To solve this issue, we adopt the synthetic depth-of-field (SYNDOF) dataset [25] for training DENet. The SYNDOF dataset contains 205 real defocused images \mathbf{I}_{real} without ground-truth defocus maps. It also contains 8,026 pairs of synthetic defocused image and defocus map $\{\mathbf{I}_{\text{syn}}, \mathbf{M}\}$. Note that \mathbf{I}_{syn} are synthesized by the thin-lens model [62] given $\hat{\mathbf{M}}$, as discussed in [25]. Then, we compress \mathbf{I}_{real} and \mathbf{I}_{syn} into real compressed images $\mathbf{I}_{\text{real}}^c$ and synthetic compressed images $\mathbf{I}_{\text{syn}}^c$, respectively. Additional details about image compression are provided in Section 5.1. Finally, we estimate the defocus maps \mathbf{M} of $\mathbf{I}_{\text{syn}}^c$ by DENet and obtain a set of $\{\mathbf{I}_{\text{syn}}^c, \hat{\mathbf{M}}, \mathbf{M}\}$ for supervision. Given the above training data of $\mathbf{I}_{\text{real}}^c$ and $\{\mathbf{I}_{\text{syn}}^c, \hat{\mathbf{M}}, \mathbf{M}\}$, we define the defocus estimation loss \mathcal{L}_{de} as follows. First, we minimize the pixelwise mean square error (MSE) between \mathbf{M} and $\hat{\mathbf{M}}$,

$$\mathcal{L}_{\text{pix}} = \|\mathbf{M} - \hat{\mathbf{M}}\|_2^2. \quad (13)$$

Then, we need to minimize the semantic distance between \mathbf{M} and $\hat{\mathbf{M}}$, measured by the featurewise MSE,

$$\mathcal{L}_{\text{feat}} = \|\phi(\mathbf{M}) - \phi(\hat{\mathbf{M}})\|_2^2, \quad (14)$$

where ϕ denotes the last convolution layer in the l -th block of a pretrained VGG-19 model [50]. Next, we focus on reducing the domain gap between $\mathbf{I}_{\text{real}}^c$ and $\mathbf{I}_{\text{syn}}^c$ during defocus estimation through the following adversarial loss [63] between their feature maps:

$$\mathcal{L}_{\text{adv}} = \alpha \cdot \log(\mathcal{D}(\psi(\mathbf{I}^c))) + (1 - \alpha) \cdot \log(1 - \mathcal{D}(\psi(\mathbf{I}^c))). \quad (15)$$

TABLE 2

Datasets adopted in this paper. The maximal image resolution (res.), image usage, and image indices of these datasets are indicated.

Dataset	Max res.	Usage	Indices
DIV2K [26]	2K	Training	0001-0800
Kodak [64]	768x512	Testing	0001-0025
DIV2K [26]	2K	Testing	0801-0900
Flickr2K [65]	2K	Testing	2551-2650
RAISE [66]	4K	Testing	8057-8156

In the above equation, \mathbf{I}^c can be either $\mathbf{I}_{\text{real}}^c$ or $\mathbf{I}_{\text{syn}}^c$; ψ denotes the last upsampling layer of DENet; \mathcal{D} is a four-layer CNN-based discriminator; α is a label, and it is equivalent to 0 when $\mathbf{I}^c = \mathbf{I}_{\text{real}}^c$ or is equivalent to 1 when $\mathbf{I}^c = \mathbf{I}_{\text{syn}}^c$. Finally, the defocus estimation loss \mathcal{L}_{de} is modeled as follows:

$$\mathcal{L}_{\text{de}} = \mathcal{L}_{\text{pix}} + \lambda_{\text{feat}} \cdot \mathcal{L}_{\text{feat}} + \lambda_{\text{adv}} \cdot \mathcal{L}_{\text{adv}}, \quad (16)$$

where λ_{feat} and λ_{adv} are the weight factors. To obtain a converged discriminator, a discriminator loss $\mathcal{L}_{\mathcal{D}} = -\mathcal{L}_{\text{adv}}$ is set to supervise the training of \mathcal{D} . Given the above loss functions, we can train DENet and the discriminator \mathcal{D} by alternately minimizing \mathcal{L}_{de} and $\mathcal{L}_{\mathcal{D}}$.

5 EXPERIMENTS

In this section, we present our experimental results to verify the performance of our proposed DAQE approach for the quality enhancement of compressed images. Since BPG (HEVC-MSP) [4], [5] and JPEG [2] are two widely used image compression codecs, our experiments focus on enhancing the quality of both BPG-compressed and JPEG-compressed images.

5.1 Experimental Setup

In this section, we present details about the datasets, hyperparameters, training strategy, and testing procedure of our DAQE approach.

Datasets. Recent works have adopted some large-scale image datasets, such as BSDS500 [68] and ImageNet [51], for image denoising, segmentation, and other image tasks. However, the images from these datasets contain unknown artifacts, since they are collected under unknown conditions and compressed by unknown codecs and settings. To obtain “clean” images without significant artifacts, we adopt several high-quality image datasets for evaluation, as illustrated in Table 2. Specifically, we adopt 800 images of the DIV2K dataset [26] as the training set. In addition, we adopt all 25 images of the Kodak dataset [64], 100 images of the DIV2K dataset, 100 images of the Flickr2K dataset [65], and 100 images of the RAISE dataset [66] as the test set. We compress all images using the BPG [5] and JPEG codecs [2]. We adopt four compression settings for each codec, *i.e.*, the quantization parameter (QP) is 27/32/37/42 in BPG and the quality factor (QF) is 20/30/40/50 in JPEG. These settings are widely used for other quality enhancement works [16], [20], [22], [69].

Hyperparameters, training and testing. In our DAQE approach, S , N_{clu} , and d are set to 128, 3, and 32, respectively. The number of attention heads is set to 3. All

TABLE 3

Quantitative comparison of our DAQE and compared approaches for BPG-compressed images. PSNR (dB) and SSIM are calculated with the BPG baseline as the anchor. Standard deviation values are presented in addition to the results. All results are calculated on the RGB channels. The PSNR and SSIM values are accurate to two and three decimal places, respectively.

Approach	QP	Kodak [64]		DIV2K [26]		Flickr2K [65]		RAISE [66]	
		PSNR	SSIM	PSNR	SSIM	PSNR	SSIM	PSNR	SSIM
Baseline	27	37.18±1.08	0.952±0.013	37.02±2.08	0.952±0.022	36.69±2.37	0.956±0.019	37.50±1.72	0.953±0.023
AR-CNN [11]		37.52±1.06	0.954±0.013	37.63±1.99	0.956±0.021	37.23±2.13	0.960±0.017	37.97±1.68	0.958±0.021
DCAD [16]		37.75±1.08	0.956±0.012	37.90±1.98	0.958±0.021	37.48±2.08	0.962±0.017	38.22±1.67	0.959±0.021
DnCNN [15]		37.79±1.09	0.956±0.012	37.91±1.96	0.958±0.021	37.49±2.08	0.962±0.017	38.23±1.67	0.959±0.021
CBDNet [67]		37.96±1.07	0.957±0.012	38.14±1.95	0.959±0.021	37.75±2.01	0.963±0.017	38.29±1.69	0.960±0.021
RBQE [20]		37.89±1.07	0.956±0.012	38.00±1.99	0.959±0.021	37.58±2.09	0.962±0.017	38.35±1.67	0.960±0.021
DAQE (Ours)		38.27±1.11	0.958±0.012	38.45±1.94	0.960±0.021	38.03±1.97	0.964±0.017	38.66±1.68	0.962±0.021
Baseline	32	33.97±1.35	0.915±0.019	34.15±2.19	0.921±0.035	33.76±2.44	0.928±0.025	34.44±1.96	0.922±0.029
AR-CNN [11]		34.32±1.35	0.919±0.019	34.72±2.15	0.927±0.034	34.26±2.34	0.934±0.024	34.92±1.94	0.928±0.027
DCAD [16]		34.53±1.39	0.921±0.019	34.96±2.17	0.929±0.034	34.48±2.35	0.936±0.023	35.11±1.95	0.930±0.027
DnCNN [15]		34.57±1.39	0.921±0.019	34.98±2.16	0.929±0.034	34.50±2.35	0.936±0.023	35.14±1.95	0.931±0.027
CBDNet [67]		34.74±1.41	0.923±0.018	35.20±2.17	0.932±0.034	34.74±2.31	0.939±0.023	35.21±1.97	0.932±0.027
RBQE [20]		34.66±1.39	0.922±0.019	35.06±2.18	0.931±0.034	34.58±2.35	0.938±0.023	35.23±1.95	0.932±0.027
DAQE (Ours)		35.06±1.46	0.925±0.018	35.51±2.19	0.934±0.034	35.02±2.30	0.941±0.023	35.56±1.98	0.935±0.026
Baseline	37	30.95±1.61	0.853±0.031	31.45±2.37	0.877±0.050	30.94±2.61	0.886±0.036	31.60±2.22	0.875±0.037
AR-CNN [11]		31.27±1.63	0.858±0.031	31.97±2.36	0.885±0.049	31.39±2.61	0.893±0.035	32.02±2.22	0.882±0.036
DCAD [16]		31.44±1.66	0.861±0.032	32.17±2.39	0.888±0.049	31.58±2.63	0.896±0.035	32.19±2.25	0.885±0.036
DnCNN [15]		31.44±1.66	0.861±0.032	32.17±2.38	0.887±0.049	31.57±2.63	0.896±0.035	32.18±2.24	0.884±0.036
CBDNet [67]		31.65±1.71	0.864±0.032	32.40±2.40	0.891±0.048	31.81±2.65	0.899±0.035	32.28±2.27	0.887±0.036
RBQE [20]		31.53±1.69	0.862±0.032	32.25±2.39	0.890±0.049	31.65±2.65	0.897±0.035	32.26±2.26	0.887±0.036
DAQE (Ours)		31.95±1.75	0.868±0.032	32.69±2.44	0.895±0.049	32.07±2.69	0.903±0.035	32.61±2.32	0.892±0.036
Baseline	42	28.36±1.87	0.766±0.055	29.04±2.61	0.817±0.065	28.35±2.88	0.822±0.054	29.07±2.53	0.809±0.056
AR-CNN [11]		28.64±1.89	0.773±0.056	29.48±2.62	0.827±0.065	28.74±2.91	0.831±0.054	29.42±2.54	0.816±0.056
DCAD [16]		28.78±1.92	0.777±0.056	29.65±2.66	0.831±0.065	28.89±2.95	0.835±0.054	29.54±2.58	0.820±0.056
DnCNN [15]		28.80±1.93	0.777±0.056	29.68±2.67	0.832±0.064	28.91±2.96	0.836±0.054	29.57±2.59	0.821±0.056
CBDNet [67]		28.96±1.97	0.781±0.057	29.87±2.71	0.836±0.064	29.10±3.01	0.840±0.054	29.60±2.61	0.822±0.056
RBQE [20]		28.85±1.95	0.778±0.057	29.71±2.67	0.833±0.065	28.94±2.99	0.837±0.055	29.60±2.61	0.822±0.057
DAQE (Ours)		29.19±2.00	0.786±0.058	30.08±2.76	0.840±0.064	29.28±3.06	0.844±0.055	29.88±2.68	0.829±0.057

convolution operators have a kernel size of 3, a stride of 1, and padding of 1. To cluster the input patches, we adopt the K-means clustering algorithm [45], [46] over the DIV2K training set. For the loss functions, we set ϵ , l , λ_{feat} , and λ_{adv} to 10^{-6} , $4 \cdot 10^{-4}$, and 10^{-3} , respectively. During the training process, the Adam [70] optimizer is applied with an initial learning rate of 10^{-4} . The cosine annealing schedule [71] is applied to decrease the learning rate automatically. The training batch size is set to 64. A workstation with one CPU (Intel Xeon Platinum 8163 CPU @ 2.50GHz) and four GPUs (Tesla V100-SXM2-16GB) is used for training and testing. We first train DENet on the training set of SYNDOF. After the convergence of DENet, we freeze the parameters of DENet and train the subsequent AGNet and QENet jointly on the DIV2K training set until convergence.

5.2 Evaluation

In this section, we evaluate the performance of our DAQE approach for the quality enhancement of compressed images. We compare our approach with several widely used approaches including AR-CNN [11], DCAD [16], DnCNN [15], CBDNet [67] and RBQE [20]. Among them, CBDNet and RBQE were originally used for blind restoration. For fair comparisons, we retrain them in a nonblind manner, *i.e.*, train one model for each compression configuration. In addition, all compared approaches are retrained

on our training set.²

Quantitative performance. To evaluate the efficacy of our DAQE approach, we measure PSNR and SSIM for different approaches on both BPG-compressed and JPEG-compressed images from four different datasets. Table 3 presents the results on BPG-compressed images. As shown in Table 3, the average PSNR of the DAQE approach on the DIV2K dataset is 32.69 dB at QP = 37, which is 1.24 dB higher than that of the BPG baseline and 0.29 dB higher than that of the second-best approach. In addition, the average SSIM is 0.895, which is 0.018 higher than the BPG baseline and 0.004 higher than that of the second-best approach. Similar results can be found for the other three datasets and other QP settings. For the JPEG-compressed images, Table 4 shows that the average PSNR of the DAQE approach on the DIV2K dataset is 34.29 dB at QF = 40, which is 2.50 dB higher than that of the JPEG baseline, and 0.35 dB higher than that of the second-best approach. In addition, the average SSIM is 0.929, which is 0.033 higher than that of the JPEG baseline and 0.003 higher than that of the second-best approach. Similar results can be found for the other three datasets and other QF settings. In summary, the DAQE approach achieves state-of-the-art performance on all four datasets for both BPG-compressed and JPEG-compressed images.

Rate-distortion performance. We further evaluate the

² Codes of all approaches are available at <https://github.com/RyanXingQL/PowerQE>.

TABLE 4

Quantitative comparison of our DAQE and compared approaches for JPEG-compressed images. PSNR (dB) and SSIM are calculated with the JPEG baseline as the anchor. Standard deviation values are presented in addition to the results. All results are calculated on the RGB channels. The PSNR and SSIM values are accurate to two and three decimal places, respectively.

Approach	QF	Kodak [64]		DIV2K [26]		Flickr2K [65]		RAISE [66]	
		PSNR	SSIM	PSNR	SSIM	PSNR	SSIM	PSNR	SSIM
Baseline	20	29.04±1.99	0.828±0.029	29.59±2.75	0.851±0.050	28.83±3.15	0.855±0.040	29.70±2.64	0.852±0.037
AR-CNN [11]		30.31±2.15	0.855±0.033	31.03±2.87	0.881±0.051	30.15±3.37	0.883±0.041	30.97±2.78	0.876±0.036
DCAD [16]		30.63±2.21	0.862±0.034	31.37±2.93	0.888±0.051	30.47±3.45	0.890±0.040	31.25±2.85	0.883±0.035
DnCNN [15]		30.71±2.23	0.863±0.034	31.45±2.93	0.888±0.051	30.54±3.47	0.891±0.040	31.32±2.86	0.884±0.035
CBDNet [67]		30.93±2.28	0.867±0.034	31.74±3.02	0.893±0.050	30.81±3.54	0.895±0.039	31.26±2.93	0.885±0.035
RBQE [20]		30.79±2.29	0.863±0.034	31.60±3.04	0.891±0.051	30.64±3.57	0.893±0.040	31.44±2.98	0.888±0.035
DAQE (Ours)		31.28±2.35	0.871±0.035	32.02±3.06	0.897±0.050	31.06±3.62	0.899±0.039	31.82±3.04	0.893±0.035
Baseline	30	30.38±2.04	0.864±0.023	30.91±2.88	0.880±0.045	30.20±3.35	0.886±0.035	31.05±2.70	0.882±0.033
AR-CNN [11]		31.65±2.19	0.885±0.025	32.37±2.98	0.904±0.045	31.51±3.48	0.908±0.034	32.31±2.80	0.902±0.030
DCAD [16]		32.00±2.25	0.892±0.026	32.73±3.03	0.910±0.045	31.85±3.54	0.914±0.033	32.62±2.87	0.908±0.029
DnCNN [15]		32.07±2.26	0.893±0.026	32.81±3.04	0.910±0.045	31.91±3.55	0.915±0.032	32.69±2.86	0.909±0.029
CBDNet [67]		32.26±2.31	0.896±0.026	33.06±3.05	0.914±0.044	32.18±3.58	0.918±0.032	32.59±2.92	0.909±0.029
RBQE [20]		32.11±2.31	0.893±0.026	32.89±3.06	0.912±0.045	31.98±3.61	0.916±0.033	32.77±2.97	0.911±0.029
DAQE (Ours)		32.64±2.38	0.900±0.026	33.39±3.09	0.918±0.044	32.47±3.63	0.922±0.032	33.18±3.00	0.916±0.029
Baseline	40	31.30±2.06	0.885±0.020	31.79±2.93	0.896±0.041	31.13±3.46	0.903±0.032	31.97±2.75	0.900±0.029
AR-CNN [11]		32.57±2.19	0.903±0.021	33.24±2.99	0.917±0.041	32.42±3.50	0.922±0.029	33.22±2.81	0.917±0.027
DCAD [16]		32.93±2.25	0.908±0.021	33.62±3.05	0.922±0.041	32.77±3.55	0.927±0.028	33.55±2.87	0.922±0.026
DnCNN [15]		33.00±2.26	0.909±0.021	33.69±3.04	0.923±0.041	32.83±3.54	0.927±0.028	33.61±2.86	0.923±0.026
CBDNet [67]		33.19±2.30	0.912±0.021	33.94±3.03	0.926±0.040	33.10±3.55	0.930±0.027	33.50±2.89	0.923±0.026
RBQE [20]		33.03±2.29	0.909±0.021	33.75±3.05	0.924±0.041	32.88±3.58	0.928±0.029	33.67±2.93	0.924±0.026
DAQE (Ours)		33.56±2.37	0.915±0.022	34.29±3.07	0.929±0.040	33.40±3.58	0.933±0.027	34.10±2.95	0.929±0.026
Baseline	50	32.05±2.04	0.899±0.017	32.49±2.94	0.909±0.038	31.89±3.62	0.915±0.030	32.70±2.74	0.912±0.027
AR-CNN [11]		33.29±2.16	0.915±0.018	33.93±2.98	0.927±0.038	33.13±3.51	0.931±0.027	33.93±2.78	0.927±0.025
DCAD [16]		33.64±2.21	0.920±0.018	34.29±3.03	0.931±0.038	33.47±3.53	0.936±0.025	34.25±2.82	0.932±0.024
DnCNN [15]		33.68±2.21	0.920±0.018	34.33±3.01	0.931±0.037	33.50±3.52	0.936±0.025	34.28±2.80	0.931±0.024
CBDNet [67]		33.91±2.27	0.923±0.018	34.61±3.01	0.934±0.037	33.81±3.51	0.939±0.024	34.22±2.84	0.932±0.024
RBQE [20]		33.72±2.25	0.920±0.018	34.40±3.02	0.932±0.037	33.56±3.56	0.937±0.025	34.35±2.87	0.933±0.024
DAQE (Ours)		34.32±2.33	0.927±0.018	35.01±3.03	0.938±0.037	34.15±3.53	0.942±0.024	34.86±2.88	0.938±0.024

TABLE 5

Rate-distortion performance of our DAQE and compared approaches. The rate-distortion performance is measured by the BD-rate reduction (%) with the BPG/JPEG baseline as the anchor. Standard deviations are presented in addition to the results. The rate is measured by the bits per pixel (BPP). The distortion is measured by PSNR (dB) and SSIM.

Approach	Kodak [64]		DIV2K [26]		Flickr2K [65]		RAISE [66]	
	BPG	JPEG	BPG	JPEG	BPG	JPEG	BPG	JPEG
BPP-PSNR								
AR-CNN [11]	-7.06±1.93	-21.22±2.93	-11.14±5.64	-23.48±6.11	-9.26±4.80	-21.26±5.26	-9.45±5.46	-20.78±5.73
DCAD [16]	-10.85±3.01	-25.88±3.91	-15.20±6.75	-28.11±7.26	-12.84±5.88	-25.66±6.31	-12.91±6.45	-24.86±6.57
DnCNN [15]	-11.24±2.98	-26.79±3.98	-15.47±6.94	-29.08±7.77	-12.99±5.94	-26.46±6.42	-13.19±6.39	-25.81±6.70
CBDNet [67]	-14.79±3.95	-29.64±4.53	-19.38±7.81	-32.53±7.79	-16.88±7.05	-29.92±7.42	-14.65±6.67	-24.77±6.82
RBQE [20]	-12.91±3.12	-27.72±4.34	-16.82±7.43	-30.92±10.02	-14.28±6.10	-27.47±6.67	-14.66±6.95	-27.16±7.28
DAQE (Ours)	-20.17±5.09	-34.22±5.65	-24.05±9.10	-35.17±10.02	-21.08±8.16	-33.01±8.21	-20.66±7.99	-32.19±8.00
BPP-SSIM								
AR-CNN [11]	-5.18±2.46	-17.48±5.67	-10.40±8.13	-22.91±10.18	-9.03±6.33	-20.57±7.64	-9.09±8.42	-17.90±7.60
DCAD [16]	-8.36±3.76	-22.36±6.62	-13.55±14.07	-28.35±12.03	-12.68±8.10	-25.59±8.72	-12.57±10.03	-22.74±8.53
DnCNN [15]	-8.25±3.71	-22.93±6.65	-14.36±8.95	-29.28±13.23	-12.23±7.73	-26.19±9.14	-12.05±9.44	-25.03±15.20
CBDNet [67]	-11.17±4.81	-25.46±7.54	-16.45±21.19	-32.58±13.57	-16.15±9.81	-29.88±10.40	-14.72±12.33	-23.71±10.94
RBQE [20]	-9.26±4.45	-23.25±7.48	-16.29±10.70	-31.17±13.81	-13.99±9.58	-28.08±11.17	-14.57±13.31	-26.44±13.78
DAQE (Ours)	-14.89±6.25	-28.65±8.74	-22.14±11.77	-34.32±12.19	-19.74±11.17	-32.50±10.81	-19.89±14.51	-30.11±13.64

rate-distortion performance of our DAQE approach in Figure 8 and Table 5. Figure 8 shows the rate-distortion curves of different approaches on the four datasets. As shown in the figure, the rate-distortion curves of our DAQE approach are higher than those of other approaches, indicating the superior rate-distortion performance of our approach. Then, we quantify the rate-distortion performance by evaluating the reduction in Bjontegaard-rate (BD-rate) [72]. The results

are presented in Table 5. As shown, for BPG-compressed images, the BD-rate reductions of our DAQE approach on the DIV2K dataset are on average 24.05% and 22.14% with the distortion measured by PSNR and SSIM, respectively, while those of the second-best approach are only 19.38% and 16.45% on average. Similar results can be observed for the other three datasets and JPEG-compressed images. In summary, our DAQE approach significantly surpasses state-

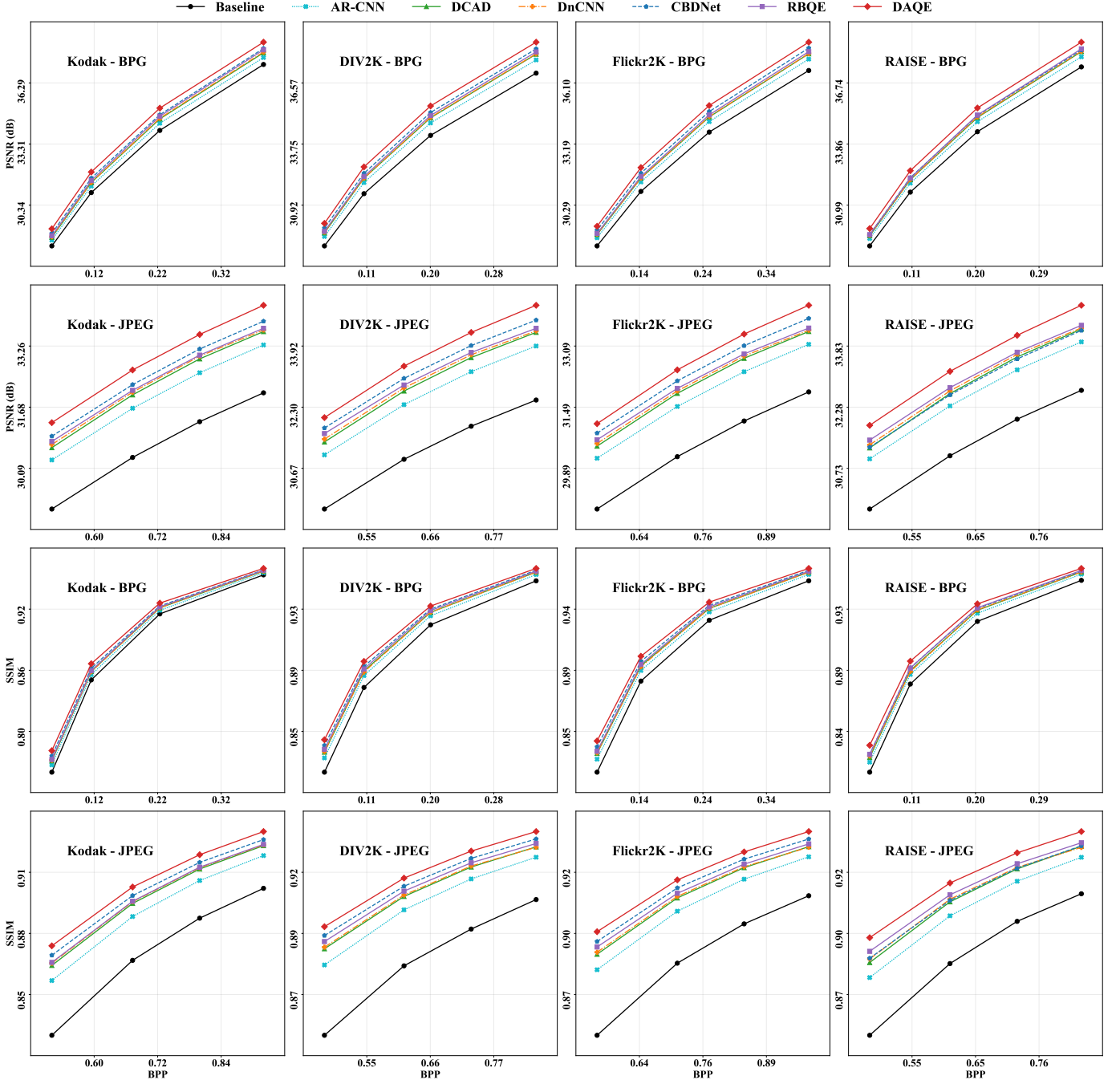


Fig. 8. Rate-distortion curves of our DAQE and compared approaches. The rate is measured by the bits per pixel (BPP). The distortion is measured by PSNR (dB) and SSIM.

of-the-art rate-distortion performance.

Qualitative performance. Figure 9 compares the visual results of our DAQE and the compared approaches. Specifically, the DAQE approach successfully restores the edge details of the door, motorbike, and window in Figure 9 (a)-(c), respectively. In contrast, these details cannot be well restored by the other approaches. In addition, the DAQE approach suppresses the compression artifacts around these edges, while those artifacts are hardly reduced by the other approaches. To summarize, the DAQE approach outperforms the compared approaches qualitatively, especially in restoring details and suppressing compression artifacts.

Efficiency. We measure the efficiency of our DAQE and other compared approaches from two aspects: the time complexity in terms of the frames per second (FPS) and the space complexity in terms of the number of parameters. As shown in Figure 10, the DAQE approach outperforms the second-best CBDNet by 0.29 dB in PSNR with 8.67% fewer parameters and 4.80% higher FPS. Some approaches, such as AR-CNN and DCAD, have fewer parameters and higher FPS than the DAQE approach and CBDNet. However, their PSNR performance is at least 0.44 dB lower than that of the DAQE approach. In summary, our DAQE approach achieves a good balance between efficiency and enhance-

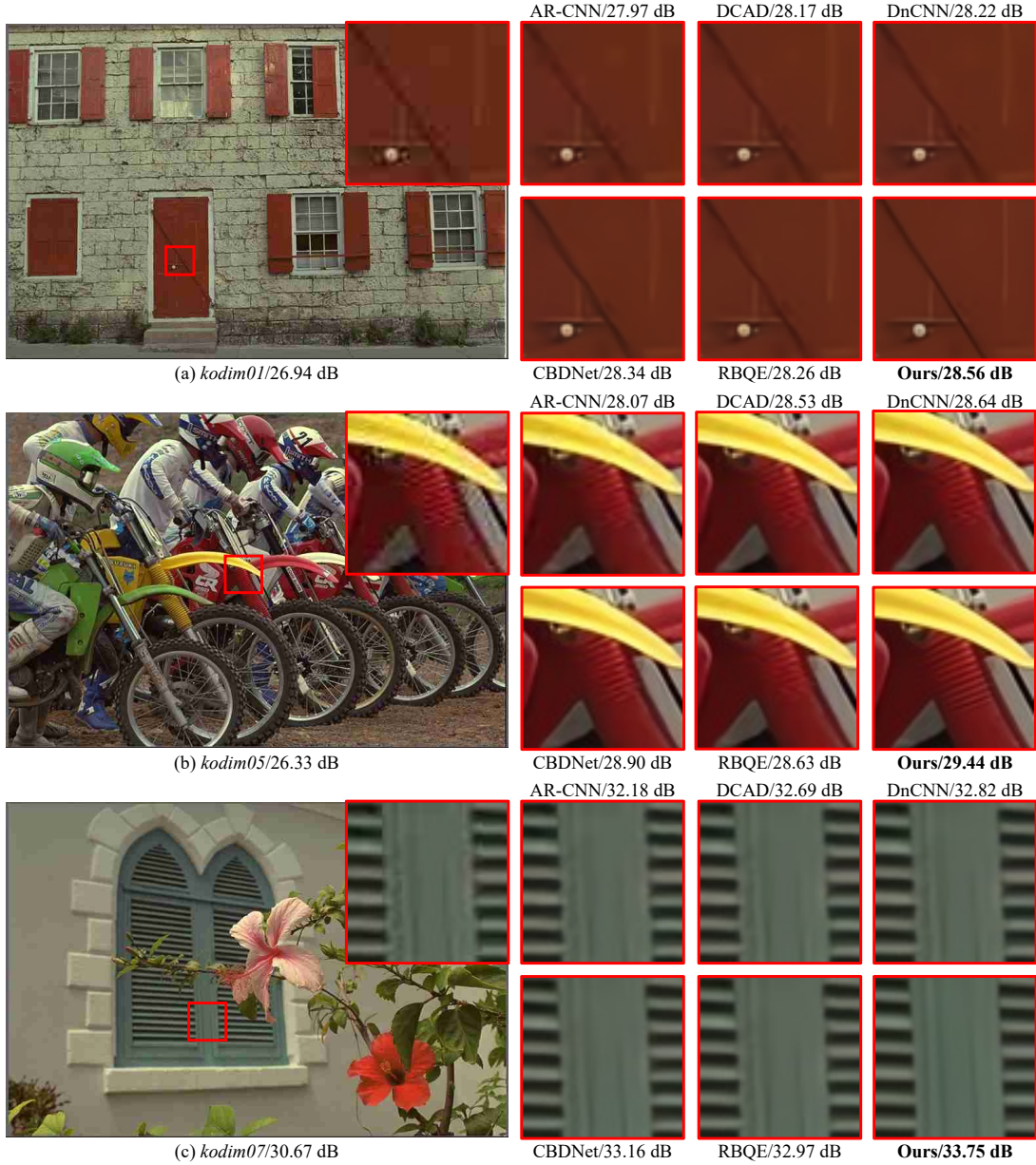


Fig. 9. Qualitative comparison of our DAQE and compared approaches.

ment performance.

Defocus estimation. To evaluate the defocus estimation performance of DENet for compressed images, we compare DENet with the state-of-the-art DMENet [25] on the CUHK dataset compressed by BPG at QP=37. In addition to the officially released model of DMENet, we also retrain DMENet on the official training set but with compression, named DMENet-Comp. Finally, we measure the accuracy of defocus estimation by each model. The average accuracy scores of DENet, DMENet, and DMENet-Comp are 81.73%, 70.96%, and 76.30%, respectively. In other words, the compression artifacts degrade the defocus estimation accuracy of the compared DMENet by 5.34%. In addition, the proposed DENet outperforms the retrained DMENet by 5.49% in accuracy on the test set. These experimental results further demonstrate the necessity of proposing DENet to estimate the defocus map for compressed images.

TABLE 6
Ablation results of our DAQE approach in terms of PSNR (dB).

Component	DAQE	(A)	(B)	(C)
Local attention of AGNet	✓	✓	✓	✗
Global attention of AGNet	✓	✓	✗	✗
CA subnet of QENet	✓	✗	✗	✗
PSNR (dB)	32.69	32.59	32.54	32.51

5.3 Ablation Study

Network components. Some important components are proposed in our DAQE network. First, a local attention module is designed in AGNet to extract the texture pattern for each input patch. In addition, AGNet is equipped with a global attention module for extracting the texture pattern of the input patch by referring to all patches in the same

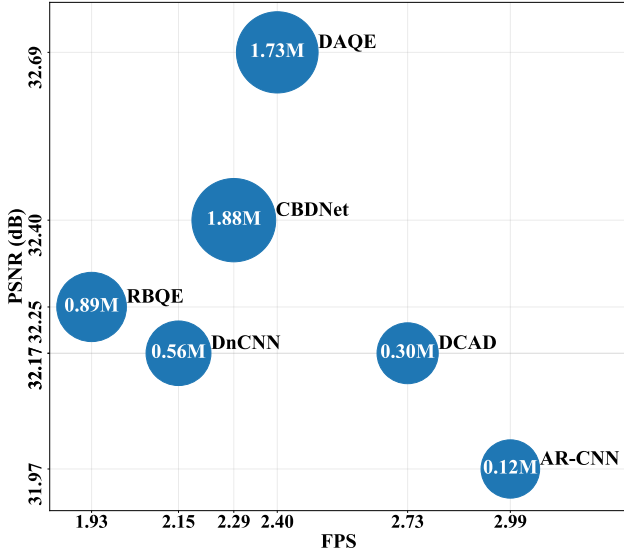


Fig. 10. Efficiency of our DAQE and compared approaches over the DIV2K test set compressed by BPG at QP = 37. The number of parameters is marked at the center of each circle. A larger circle radius indicates a larger number of parameters.

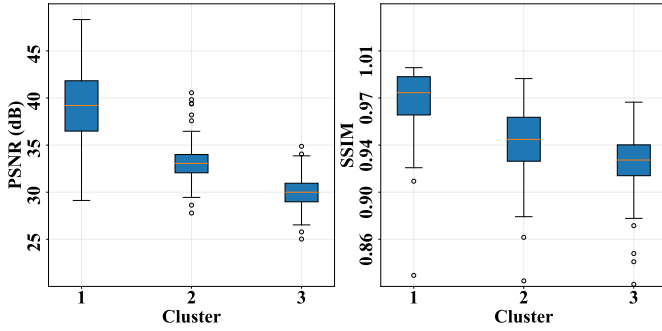


Fig. 11. Statistics of PSNR and SSIM values for patches in different clusters. Patches are from the DIV2K test set compressed by BPG at QP = 37.

cluster. Finally, the CA subnet is proposed to effectively connect each level of QENet. To validate the effectiveness of these network components, we gradually ablate each component to generate three different networks denoted by (A) to (C), as presented in Table 6. Then, we retrain and test all these networks on the DIV2K dataset compressed by BPG at QP = 37. As shown in Table 6, ablating the CA subnets degrades PSNR by 0.10 dB. Further ablations of the global attention and local attention lead to 0.05 and 0.03 dB degradation in PSNR, respectively. Thus, these network components have a positive influence on the enhancement performance of the DAQE approach.

Defocus-based patch classification. During the process of defocus-based patch classification, we classify the patches into three different clusters by DENet, to prepare for subsequent dynamic quality enhancement. Figure 11 shows the statistics of the patches after defocus estimation and clustering. Patches from different clusters significantly differ in compression quality in terms of both the PSNR and SSIM values. Specifically, the median PSNR values of the patches in the three clusters are 39.21, 33.06, and 30.00

dB. The median SSIM values of the patches in the three clusters are 0.98, 0.94, and 0.92. Large quality gaps between patches in different clusters bring great benefits to cluster-specific quality enhancement. Notably, the classification of compressed patches in our DAQE approach does not rely on raw patches, making it practical in real-world applications.

We also measure the upper bound for our DAQE approach (*i.e.*, DAQE-Upper) by computing the compression quality of patches in terms of PSNR and then clustering patches according to their quality. Note that we retrain DAQE-Upper on the training set. Experimental results show that DAQE-Upper achieves an average PSNR of 32.84 dB, which further improves the performance of DAQE (*i.e.*, 32.69 dB) by 0.15 dB. This experiment provides the upper bound for DAQE and demonstrates the effectiveness of enhancing patches with different quality in a divide-and-conquer manner. More importantly, by reasoning about image defocus, DAQE can efficiently cluster patches with different quality without requiring raw patches. In summary, the above experiment demonstrates the effectiveness of using defocus for quality enhancement in the aspect of clustering patches with different quality.

Defocus-based attention. To evaluate the effectiveness of defocus-based attention, we design a defocus-blind quality enhancement approach, called DAQE-Blind, with the following modifications to DAQE. (1) First, all reference patches are used for the global attention module, since there is only one cluster and all reference patches are adopted for this cluster. (2) Second, all patches are forced to exit at a fixed level of QENet, because DAQE-Blind cannot manage the dynamic inference of DAQE without knowing the defocus information. For a fair comparison, we exit all patches at the first level of QENet for DAQE-Blind and DAQE. We then train these two approaches on our training set and evaluate their performance.

We measure the PSNR-FPS performance of these two approaches. DAQE-Blind achieves an average PSNR of 32.47 dB, which is slightly worse than DAQE (*i.e.*, 32.56 dB). In other words, the enhanced PSNR degrades by 8.11% for DAQE-Blind compared with DAQE, *i.e.*, 1.02 vs. 1.11 dB. More importantly, the FPS results of DAQE-Blind and DAQE are 1.85 and 2.81, respectively, indicating a speed degradation of 34.16% for DAQE-Blind over DAQE. The reason for this degradation is that DAQE uses only a few reference patches with similar quality and texture, but all reference patches are presented to DAQE-Blind, making it more difficult for DAQE-Blind to find relevance from a large number of patches and then learn from those patches. In summary, it is necessary to exploit the defocus characteristic of image patches in our approach in terms of both effectiveness and efficiency.

Finally, we measure the correlation between defocus differences and attention ranks for each input patch of DAQE-Blind. Specifically, the defocus differences are measured between the input patch and all reference patches; the attention ranks are obtained by referring to the attention values of the reference patches. The experimental result shows that the PCC value can reach 0.74 on average. Therefore, the attended patches by DAQE-Blind are similar to the input patch in terms of defocus. In other words, a small number of patches with similar defocus values can serve as effective

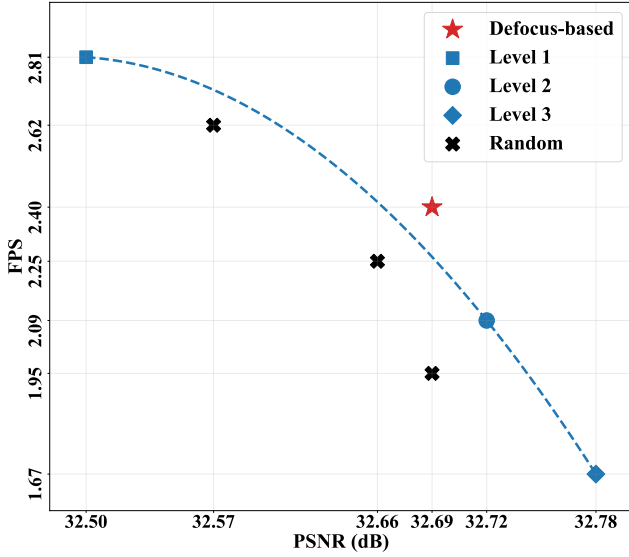


Fig. 12. PSNR-FPS performance of different enhancement strategies over the DIV2K test set compressed by BPG at QP = 37.

tive references for quality enhancement to find regionwise relevance. The above experiments show the effectiveness of using defocus for quality enhancement in the aspect of finding regionwise relevance.

Defocus-based dynamic enhancement. To evaluate the efficacy of the defocus-based dynamic enhancement of the DAQE approach, we design the following experiments. Specifically, instead of the defocus-based dynamic enhancement, we compulsively exit all patches at the first level of QENet without considering their defocus values. All patches are treated in a single cluster and all reference patches are used for the global attention module. The PSNR-FPS result is denoted by the blue square in Figure 12. Similarly, all patches exit at the second and the third levels of QENet separately, generating two PSNR-FPS results also shown in Figure 12. Finally, each patch randomly exits with three different random seeds, generating three PSNR-FPS results, as shown in Figure 12. As shown, compared with other strategies, our defocus-based dynamic enhancement (denoted by the red star) achieves a superior tradeoff between enhancement quality and speed.

Frequency-based clustering. The quality and texture pattern of compressed patches are also related to their frequency content. Therefore, we equip the proposed image restoration architecture with frequency detection and frequency-based patch clustering and then verify its performance. The resulting approach is denoted by DAQE-Freq. Specifically, DAQE-Freq computes the wavelet energy [73] of image patches and then clusters the patches according to their energy. Here, the wavelet energy is computed as the summed squares of the wavelet coefficients of the high-frequency subbands, *i.e.*, LH, HL, and HH. We then train DAQE-Freq on our training set.

We measure the PSNR performance of DAQE-Freq. The average PSNR over the test set is 32.52 dB, which is 0.17 dB lower than that of DAQE (*i.e.*, 32.69 dB). We also find that the average PCC value between the detected frequency and PSNR values is 0.70, which is worse than that between the

estimated defocus and PSNR values (*i.e.*, 0.78). The reason is that the frequency detection is performed on the compressed patches and is thus affected by compression artifacts. To demonstrate this fact, we feed DAQE-Freq with the “clean” wavelet energy of raw patches and then retrain DAQE-Freq. The PCC value increases from 0.70 to 0.76, and the PSNR increases from 32.52 dB to 32.62 dB. Note that the raw patches cannot be obtained in practice during enhancement. In summary, simply replacing the defocus estimation with frequency detection degrades the performance of our DAQE approach for enhancing the quality of compressed images.

6 CONCLUSION

In this paper, we proposed the defocus-aware quality enhancement (DAQE) approach. Our DAQE approach considers the regionwise defocus difference of compressed images, thus differing from the traditional quality enhancement approaches in two aspects. (1) The DAQE approach employs fewer computational resources to enhance the quality of significantly defocused regions and more resources to enhance the quality of other regions. (2) The DAQE approach learns to separately enhance diverse texture patterns for regions with different defocus values, such that texture-specific enhancement can be managed. To achieve these goals, the DAQE approach first estimates the defocus value for each image region with the proposed DENet. Next, patches are classified into different clusters according to their defocus values and then sent to AGNet and QENet to accomplish cluster-specific texture extraction and dynamic quality enhancement. Finally, extensive experiments validated that our DAQE approach can significantly improve the quality of compressed images in a resource-efficient manner and is superior to existing state-of-the-art approaches.

We propose two research directions for future work. (1) Our work considers PSNR and SSIM as the metrics for compression quality to be enhanced. Future work could embrace other perceptual quality metrics to improve the QoE of compressed images since the image defocus also correlates with the perceptual quality of compressed images. (2) Our work focuses on the quality enhancement of compressed images. Future work may extend the scope of defocus-aware approaches to other image enhancement and restoration tasks, *e.g.*, image denoising and deblurring, because image defocus is inherent in the physics of image formation and can be utilized by more low-level vision tasks.

REFERENCES

- [1] D. Inc., “Data Never Sleeps 8.0: How much data is generated every minute?” 2020.
- [2] G. Wallace, “The JPEG still picture compression standard,” *IEEE Transactions on Consumer Electronics*, vol. 38, no. 1, pp. xviii–xxxiv, 1992.
- [3] M. Marcellin, M. Gormish, A. Bilgin, and M. Boliek, “An overview of JPEG-2000,” in *Proceedings DCC 2000. Data Compression Conference*. IEEE Comput. Soc, 2000.
- [4] G. J. Sullivan, J.-R. Ohm, W.-J. Han, and T. Wiegand, “Overview of the high efficiency video coding (HEVC) standard,” *IEEE Transactions on Circuits and Systems for Video Technology*, vol. 22, no. 12, pp. 1649–1668, Dec. 2012.
- [5] F. Bellard, “Better portable graphics (BPG),” 2018.
- [6] M.-Y. Shen and C. C. J. Kuo, “Review of Postprocessing Techniques for Compression Artifact Removal,” *Journal of Visual Communication and Image Representation*, vol. 9, no. 1, pp. 2–14, Mar. 1998.

- [7] K. Seshadrinathan, R. Soundararajan, A. C. Bovik, and L. K. Cormack, "Study of subjective and objective quality assessment of video," *IEEE Transactions on Image Processing*, vol. 19, no. 6, pp. 1427–1441, Jun. 2010.
- [8] I. T. U. C. S. S. (ITU-T), "P.10 : Vocabulary for performance, quality of service and quality of experience," Nov. 2017.
- [9] N. Salvaggio, *Basic Photographic Materials and Processes*. Routledge, Apr. 2013.
- [10] M. Kraus and M. Strengert, "Depth-of-field rendering by pyramidal image processing," *Computer Graphics Forum*, vol. 26, no. 3, pp. 645–654, Sep. 2007.
- [11] C. Dong, Y. Deng, C. C. Loy, and X. Tang, "Compression artifacts reduction by a deep convolutional network," in *2015 IEEE International Conference on Computer Vision (ICCV)*. IEEE, Dec. 2015.
- [12] J. Guo and H. Chao, "Building dual-domain representations for compression artifacts reduction," in *Computer Vision – ECCV 2016*. Springer International Publishing, 2016, pp. 628–644.
- [13] Z. Wang, D. Liu, S. Chang, Q. Ling, Y. Yang, and T. S. Huang, "D3: Deep dual-domain based fast restoration of JPEG-Compressed images," in *2016 IEEE Conference on Computer Vision and Pattern Recognition (CVPR)*. IEEE, Jun. 2016.
- [14] L. Galteri, L. Seidenari, M. Bertini, and A. D. Bimbo, "Deep generative adversarial compression artifact removal," in *2017 IEEE International Conference on Computer Vision (ICCV)*. IEEE, Oct. 2017.
- [15] K. Zhang, W. Zuo, Y. Chen, D. Meng, and L. Zhang, "Beyond a gaussian denoiser: Residual learning of deep CNN for image denoising," *IEEE Transactions on Image Processing*, vol. 26, no. 7, pp. 3142–3155, Jul. 2017.
- [16] T. Wang, M. Chen, and H. Chao, "A novel deep learning-based method of improving coding efficiency from the decoder-end for HEVC," in *2017 Data Compression Conference (DCC)*. IEEE, Apr. 2017.
- [17] J. Guo and H. Chao, "One-to-many network for visually pleasing compression artifacts reduction," in *2017 IEEE Conference on Computer Vision and Pattern Recognition (CVPR)*. IEEE, Jul. 2017.
- [18] Q. Mao, S. Wang, S. Wang, X. Zhang, and S. Ma, "Enhanced image decoding via edge-preserving generative adversarial networks," in *2018 IEEE International Conference on Multimedia and Expo (ICME)*. IEEE, Jul. 2018.
- [19] Q. Mao, S. Wang, X. Zhang, S. Wang, and S. Ma, "Fidelity or quality? A region-aware framework for enhanced image decoding via hybrid neural networks," in *2019 IEEE International Conference on Image Processing (ICIP)*. IEEE, Sep. 2019.
- [20] Q. Xing, M. Xu, T. Li, and Z. Guan, "Early exit or not: Resource-efficient blind quality enhancement for compressed images," in *Computer Vision – ECCV 2020 - 16th European Conference, Glasgow, UK, August 23-28, 2020, Proceedings, Part XVI*, ser. Lecture Notes in Computer Science, A. Vedaldi, H. Bischof, T. Brox, and J.-M. Frahm, Eds., vol. 12361. Springer, 2020, pp. 275–292.
- [21] J. Deng, L. Wang, S. Pu, and C. Zhuo, "Spatio-Temporal Deformable Convolution for Compressed Video Quality Enhancement," *Proceedings of the AAAI Conference on Artificial Intelligence*, vol. 34, no. 07, pp. 10 696–10 703, Apr. 2020.
- [22] Z. Guan, Q. Xing, M. Xu, R. Yang, T. Liu, and Z. Wang, "MFQE 2.0: A New Approach for Multi-frame Quality Enhancement on Compressed Video," *IEEE Transactions on Pattern Analysis and Machine Intelligence*, vol. 43, no. 3, pp. 949–963, Mar. 2021.
- [23] M. Zheng, Q. Xing, M. Qiao, M. Xu, L. Jiang, H. Liu, and Y. Chen, "Progressive Training of A Two-Stage Framework for Video Restoration," in *2022 IEEE/CVF Conference on Computer Vision and Pattern Recognition Workshops (CVPRW)*. New Orleans, LA, USA: IEEE, Jun. 2022, pp. 1023–1030.
- [24] R. Yang, R. Timofte, M. Zheng, Q. Xing, M. Qiao, M. Xu, L. Jiang, H. Liu, Y. Chen, Y. Ben, X. Zhou, C. Fu, P. Cheng, G. Yu, J. Li, R. Wu, Z. Zhang, W. Shang, Z. Lv, Y. Chen, M. Zhou, D. Ren, K. Zhang, W. Zuo, P. Ostyakov, V. Dmitry, S. Soltanayev, C. Sergey, Z. Magaiya, X. Zou, Y. Yan, P. Navarrete Michelini, Y. Lu, D. Zhang, S. Liu, S. Gao, B. Wu, C. Zheng, X. Zhang, K. Lu, N. Wang, T. Nguyen Canh, T. Bach, Q. Wang, X. Sun, H. Ma, S. Zhao, J. Li, L. Xie, S. Shi, Y. Yang, X. Wang, J. Gu, C. Dong, X. Shi, C. Nian, D. Jiang, J. Lin, Z. Xie, M. Ye, D. Luo, L. Peng, S. Chen, X. Liu, Q. Wang, X. Liu, B. Liang, H. Dong, Y. Huang, K. Chen, X. Guo, Y. Sun, H. Wu, P. Wei, Y. Huang, J. Chen, I. Hyun Lee, S. Ali Khawaja, and J. Yoon, "NTIRE 2022 Challenge on Super-Resolution and Quality Enhancement of Compressed Video: Dataset, Methods and Results," in *2022 IEEE/CVF Conference on Computer Vision and Pattern Recognition Workshops (CVPRW)*. New Orleans, LA, USA: IEEE, Jun. 2022, pp. 1220–1237.
- [25] J. Lee, S. Lee, S. Cho, and S. Lee, "Deep defocus map estimation using domain adaptation," in *IEEE Conference on Computer Vision and Pattern Recognition, CVPR 2019, Long Beach, CA, USA, June 16-20, 2019*. Computer Vision Foundation / IEEE, 2019, pp. 12 222–12 230.
- [26] E. Agustsson and R. Timofte, "NTIRE 2017 challenge on single image super-resolution: Dataset and study," in *2017 IEEE Conference on Computer Vision and Pattern Recognition Workshops, CVPR Workshops 2017, Honolulu, HI, USA, July 21-26, 2017*. IEEE Computer Society, 2017, pp. 1122–1131.
- [27] Y. LeCun, Y. Bengio, and G. Hinton, "Deep learning," *Nature*, vol. 521, no. 7553, pp. 436–444, May 2015.
- [28] K. He, X. Zhang, S. Ren, and J. Sun, "Deep residual learning for image recognition," in *2016 IEEE Conference on Computer Vision and Pattern Recognition (CVPR)*. IEEE, Jun. 2016.
- [29] S. Ioffe and C. Szegedy, "Batch normalization: Accelerating deep network training by reducing internal covariate shift," in *Proceedings of the 32nd International Conference on Machine Learning, ICML 2015, Lille, France, 6-11 July 2015*, ser. JMLR Workshop and Conference Proceedings, F. R. Bach and D. M. Blei, Eds., vol. 37. JMLR.org, 2015, pp. 448–456.
- [30] K. Dabov, A. Foi, V. Katkovnik, and K. Egiazarian, "Image denoising by sparse 3-D transform-domain collaborative filtering," *IEEE Transactions on Image Processing*, vol. 16, no. 8, pp. 2080–2095, Aug. 2007.
- [31] A. P. Pentland, "Depth of scene from depth of field," SRI INTERNATIONAL MENLO PARK CA, Tech. Rep., 1982.
- [32] D. Ziou and F. Deschenes, "Depth from defocus estimation in spatial domain," *Computer Vision and Image Understanding*, vol. 81, no. 2, pp. 143–165, Feb. 2001.
- [33] S. Gur and L. Wolf, "Single image depth estimation trained via depth from defocus cues," in *2019 IEEE/CVF Conference on Computer Vision and Pattern Recognition (CVPR)*. IEEE, Jun. 2019.
- [34] M. Maximov, K. Galim, and L. Leal-Taixe, "Focus on defocus: Bridging the synthetic to real domain gap for depth estimation," in *2020 IEEE/CVF Conference on Computer Vision and Pattern Recognition (CVPR)*. IEEE, Jun. 2020.
- [35] T. Gureyev, A. Stevenson, Y. Nesterets, and S. Wilkins, "Image deblurring by means of defocus," *Optics Communications*, vol. 240, no. 1-3, pp. 81–88, Oct. 2004.
- [36] C. Zhou and S. Nayar, "What are good apertures for defocus deblurring?" in *2009 IEEE International Conference on Computational Photography (ICCP)*. IEEE, Apr. 2009.
- [37] X. Zhang, R. Wang, X. Jiang, W. Wang, and W. Gao, "Spatially variant defocus blur map estimation and deblurring from a single image," *Journal of Visual Communication and Image Representation*, vol. 35, pp. 257–264, Feb. 2016.
- [38] Z. Chen, J. Yuan, and Y.-P. Tan, "Hybrid saliency detection for images," *IEEE Signal Processing Letters*, vol. 20, no. 1, pp. 95–98, Jan. 2013.
- [39] P. Jiang, H. Ling, J. Yu, and J. Peng, "Salient region detection by UFO: Uniqueness, focusness and objectness," in *2013 IEEE International Conference on Computer Vision*. IEEE, Dec. 2013.
- [40] C. Swain and T. Chen, "Defocus-based image segmentation," in *1995 International Conference on Acoustics, Speech, and Signal Processing*. IEEE, 1995.
- [41] B. Everitt and A. Skovrdal, *The Cambridge Dictionary of Statistics*. Cambridge: Cambridge University Press, 2011.
- [42] Z. Wang, A. C. Bovik, H. R. Sheikh, and E. P. Simoncelli, "Image quality assessment: From error visibility to structural similarity," *IEEE Trans. Image Process.*, vol. 13, no. 4, pp. 600–612, 2004.
- [43] K. Pearson, "VII. Note on regression and inheritance in the case of two parents," *Proceedings of the Royal Society of London*, vol. 58, no. 347-352, pp. 240–242, Dec. 1895.
- [44] C. Spearman, "The proof and measurement of association between two things," *The American Journal of Psychology*, vol. 15, no. 1, p. 72, Jan. 1904.
- [45] S. P. Lloyd, "Least squares quantization in PCM," *IEEE Trans. Inf. Theory*, vol. 28, no. 2, pp. 129–136, 1982.
- [46] F. Pedregosa, G. Varoquaux, A. Gramfort, V. Michel, B. Thirion, O. Grisel, M. Blondel, P. Prettenhofer, R. Weiss, V. Dubourg, J. Vanderplas, A. Passos, D. Cournapeau, M. Brucher, M. Perrot, and E. Duchesnay, "Scikit-learn: Machine learning in Python," *Journal of Machine Learning Research*, vol. 12, pp. 2825–2830, 2011.

- [47] L. A. Gatys, A. S. Ecker, and M. Bethge, "Texture synthesis using convolutional neural networks," in *Advances in Neural Information Processing Systems 28: Annual Conference on Neural Information Processing Systems 2015, December 7-12, 2015, Montreal, Quebec, Canada*, C. Cortes, N. D. Lawrence, D. D. Lee, M. Sugiyama, and R. Garnett, Eds., 2015, pp. 262–270.
- [48] X. Snelgrove, "High-resolution multi-scale neural texture synthesis," in *SIGGRAPH Asia 2017 Technical Briefs*, 2017, pp. 1–4.
- [49] V. Nair and G. E. Hinton, "Rectified linear units improve restricted boltzmann machines," in *Proceedings of the 27th International Conference on Machine Learning (ICML-10)*, June 21-24, 2010, Haifa, Israel, J. Fürnkranz and T. Joachims, Eds. Omnipress, 2010, pp. 807–814.
- [50] K. Simonyan and A. Zisserman, "Very deep convolutional networks for large-scale image recognition," in *3rd International Conference on Learning Representations, ICLR 2015, San Diego, CA, USA, May 7-9, 2015, Conference Track Proceedings*, Y. Bengio and Y. LeCun, Eds., 2015.
- [51] J. Deng, W. Dong, R. Socher, L.-J. Li, K. Li, and L. Fei-Fei, "ImageNet: A large-scale hierarchical image database," in *2009 IEEE Computer Society Conference on Computer Vision and Pattern Recognition (CVPR 2009)*, 20-25 June 2009, Miami, Florida, USA. IEEE Computer Society, 2009, pp. 248–255.
- [52] O. Ronneberger, P. Fischer, and T. Brox, "U-net: Convolutional networks for biomedical image segmentation," in *Lecture Notes in Computer Science*. Springer International Publishing, 2015, pp. 234–241.
- [53] A. Vaswani, N. Shazeer, N. Parmar, J. Uszkoreit, L. Jones, A. N. Gomez, L. Kaiser, and I. Polosukhin, "Attention is all you need," in *Advances in Neural Information Processing Systems 30: Annual Conference on Neural Information Processing Systems 2017, December 4-9, 2017, Long Beach, CA, USA*, I. Guyon, U. von Luxburg, S. Bengio, H. M. Wallach, R. Fergus, S. V. N. Vishwanathan, and R. Garnett, Eds., 2017, pp. 5998–6008.
- [54] Y. Zhang, K. Li, K. Li, L. Wang, B. Zhong, and Y. Fu, "Image super-resolution using very deep residual channel attention networks," in *Computer Vision - ECCV 2018 - 15th European Conference, Munich, Germany, September 8-14, 2018, Proceedings, Part VII*, ser. Lecture Notes in Computer Science, V. Ferrari, M. Hebert, C. Sminchisescu, and Y. Weiss, Eds., vol. 11211. Springer, 2018, pp. 294–310.
- [55] X. Wang, K. Yu, C. Dong, and C. C. Loy, "Recovering realistic texture in image super-resolution by deep spatial feature transform," in *2018 IEEE Conference on Computer Vision and Pattern Recognition, CVPR 2018, Salt Lake City, UT, USA, June 18-22, 2018*. Computer Vision Foundation / IEEE Computer Society, 2018, pp. 606–615.
- [56] T. Park, M.-Y. Liu, T.-C. Wang, and J.-Y. Zhu, "Semantic image synthesis with spatially-adaptive normalization," in *IEEE Conference on Computer Vision and Pattern Recognition, CVPR 2019, Long Beach, CA, USA, June 16-20, 2019*. Computer Vision Foundation / IEEE, 2019, pp. 2337–2346.
- [57] L. Yang, C. Liu, P. Wang, S. Wang, P. Ren, S. Ma, and W. Gao, "HiFaceGAN: Face Renovation via Collaborative Suppression and Replenishment," in *Proceedings of the 28th ACM International Conference on Multimedia*, Oct. 2020, pp. 1551–1560.
- [58] S. W. Zamir, A. Arora, S. H. Khan, M. Hayat, F. S. Khan, M.-H. Yang, and L. Shao, "Multi-stage progressive image restoration," in *IEEE Conference on Computer Vision and Pattern Recognition, CVPR 2021, Virtual, June 19-25, 2021*. Computer Vision Foundation / IEEE, 2021, pp. 14821–14831.
- [59] Z. Xia, X. Pan, S. Song, L. E. Li, and G. Huang, "Vision transformer with deformable attention," *CoRR*, vol. abs/2201.00520, 2022.
- [60] D. Hendrycks and K. Gimpel, "Gaussian error linear units (gelus)," *arXiv preprint arXiv:1606.08415*, 2016.
- [61] P. Charbonnier, L. Blanc-Féraud, G. Aubert, and M. Barlaud, "Two deterministic half-quadratic regularization algorithms for computed imaging," in *Proceedings 1994 International Conference on Image Processing, Austin, Texas, USA, November 13-16, 1994*. IEEE Computer Society, 1994, pp. 168–172.
- [62] M. Potmesil and I. Chakravarty, "A lens and aperture camera model for synthetic image generation," in *Proceedings of the 8th Annual Conference on Computer Graphics and Interactive Techniques, SIGGRAPH 1981, Dallas, Texas, USA, August 3-7, 1981*, D. Green, T. Lucido, and H. Fuchs, Eds. ACM, 1981, pp. 297–305.
- [63] I. Goodfellow, J. Pouget-Abadie, M. Mirza, B. Xu, D. Warde-Farley, S. Ozair, A. Courville, and Y. Bengio, "Generative adversarial nets," in *Advances in Neural Information Processing Systems*, Z. Ghahramani, M. Welling, C. Cortes, N. Lawrence, and K. Q. Weinberger, Eds., vol. 27. Curran Associates, Inc., 2014.
- [64] Kodak, "Kodak lossless true color image suite," Nov. 1999.
- [65] R. Timofte, E. Agustsson, L. V. Gool, M.-H. Yang, L. Zhang, B. Lim, S. Son, H. Kim, S. Nah, K. M. Lee, X. Wang, Y. Tian, K. Yu, Y. Zhang, S. Wu, C. Dong, L. Lin, Y. Qiao, C. C. Loy, W. Bae, J. J. Yoo, Y. Han, J. C. Ye, J.-S. Choi, M. Kim, Y. Fan, J. Yu, W. Han, D. Liu, H. Yu, Z. Wang, H. Shi, X. Wang, T. S. Huang, Y. Chen, K. Zhang, W. Zuo, Z. Tang, L. Luo, S. Li, M. Fu, L. Cao, W. Heng, G. Bui, T. Le, Y. Duan, D. Tao, R. Wang, X. Lin, J. Pang, J. Xu, Y. Zhao, X. Xu, J.-s. Pan, D. Sun, Y. Zhang, X. Song, Y. Dai, X. Qin, X.-P. Huynh, T. Guo, H. S. Mousavi, T. H. Vu, V. Monga, C. Cruz, K. O. Egiazarian, V. Katkovnik, R. Mehta, A. K. Jain, A. Agarwalla, C. V. S. Praveen, R. Zhou, H. Wen, C. Zhu, Z. Xia, Z. Wang, and Q. Guo, "NTIRE 2017 challenge on single image super-resolution: Methods and results," in *2017 IEEE Conference on Computer Vision and Pattern Recognition Workshops, CVPR Workshops 2017, Honolulu, HI, USA, July 21-26, 2017*. IEEE Computer Society, 2017, pp. 1110–1121.
- [66] D.-T. Dang-Nguyen, C. Pasquini, V. Conotter, and G. Boato, "RAISE: A raw images dataset for digital image forensics," in *Proceedings of the 6th ACM Multimedia Systems Conference, MMSys 2015, Portland, OR, USA, March 18-20, 2015*, W. T. Ooi, W.-c. Feng, and F. Liu, Eds. ACM, 2015, pp. 219–224.
- [67] S. Guo, Z. Yan, K. Zhang, W. Zuo, and L. Zhang, "Toward convolutional blind denoising of real photographs," in *2019 IEEE/CVF Conference on Computer Vision and Pattern Recognition (CVPR)*. IEEE, Jun. 2019.
- [68] P. Arbelaez, M. Maire, C. Fowlkes, and J. Malik, "Contour detection and hierarchical image segmentation," *IEEE Transactions on Pattern Analysis and Machine Intelligence*, vol. 33, no. 5, pp. 898–916, May 2011.
- [69] R. Yang, M. Xu, Z. Wang, and T. Li, "Multi-frame quality enhancement for compressed video," in *2018 IEEE/CVF Conference on Computer Vision and Pattern Recognition*. IEEE, Jun. 2018.
- [70] D. P. Kingma and J. Ba, "Adam: A method for stochastic optimization," 2017.
- [71] I. Loshchilov and F. Hutter, "SGDR: Stochastic gradient descent with warm restarts," in *5th International Conference on Learning Representations, ICLR 2017, Toulon, France, April 24-26, 2017, Conference Track Proceedings*. OpenReview.net, 2017.
- [72] G. Bjontegaard, "Calculation of average PSNR differences between RD-curves," *VCEG-M33*, 2001.
- [73] J. Wang, M. Xu, X. Deng, L. Shen, and Y. Song, "MW-GAN+ for Perceptual Quality Enhancement on Compressed Video," *IEEE Transactions on Circuits and Systems for Video Technology*, vol. 32, no. 7, pp. 4224–4237, Jul. 2022.